Volume 146 October 2014 ISSN 0022-4073
website: http://www.elsevier.com/locate/jqsrt

ELSEVIER

Journal of
Quantitative
Spectroscopy &
Radiative
Transfer

SPECIAL ISSUE

ELECTROMAGNETIC AND LIGHT SCATTERING BY NONSPHERICAL PARTICLES XIV

Guest Editors:
Oleg Dubovik, Laurent Labonnote, Pavel Litvinov, Frédéric Parol, Michael I. Mishchenko

Journal of Quantitative Spectroscopy & Radiative Transfer 146 (2014) 510–528

Contents lists available at ScienceDirect

Journal of Quantitative Spectroscopy & Radiative Transfer

journal homepage: www.elsevier.com/locate/jqsrt

A numerical testbed for remote sensing of aerosols, and its demonstration for evaluating retrieval synergy from a geostationary satellite constellation of GEO-CAPE and GOES-R

Jun Wang [a,*], Xiaoguang Xu [a], Shouguo Ding [a], Jing Zeng [a], Robert Spurr [b], Xiong Liu [c], Kelly Chance [c], Michael Mishchenko [d]

[a] Department of Earth and Atmospheric Sciences, University of Nebraska – Lincoln, 303 Bessey Hall, Lincoln, NE 68588, USA
[b] RT Solutions, Inc., Cambridge, MA 02138, USA
[c] Harvard-Smithsonian Center for Astrophysics, 60 Garden Street, Cambridge, MA 02138, USA
[d] NASA Goddard Institute for Space Studies, 2880 Broadway, New York, NY 10025, USA

ARTICLE INFO

Article history:
Received 8 January 2014
Received in revised form
18 March 2014
Accepted 20 March 2014
Available online 29 March 2014

Keywords:
Testbed of remote sensing of aerosols
GEO-CAPE
TEMPO
GOES-R
Optimization
Linearized codes for radiative transfer and scattering

ABSTRACT

We present a numerical testbed for remote sensing of aerosols, together with a demonstration for evaluating retrieval synergy from a geostationary satellite constellation. The testbed combines inverse (optimal-estimation) software with a forward model containing linearized code for computing particle scattering (for both spherical and non-spherical particles), a kernel-based (land and ocean) surface bi-directional reflectance facility, and a linearized radiative transfer model for polarized radiance. Calculation of gas absorption spectra uses the HITRAN (HIgh-resolution TRANsmission molecular absorption) database of spectroscopic line parameters and other trace species cross-sections. The outputs of the testbed include not only the Stokes 4-vector elements and their sensitivities (Jacobians) with respect to the aerosol single scattering and physical parameters (such as size and shape parameters, refractive index, and plume height), but also DFS (Degree of Freedom for Signal) values for retrieval of these parameters. This testbed can be used as a tool to provide an objective assessment of aerosol information content that can be retrieved for any constellation of (planned or real) satellite sensors and for any combination of algorithm design factors (in terms of wavelengths, viewing angles, radiance and/or polarization to be measured or used). We summarize the components of the testbed, including the derivation and validation of analytical formulae for Jacobian calculations. Benchmark calculations from the forward model are documented. In the context of NASA's Decadal Survey Mission GEO-CAPE (GEOstationary Coastal and Air Pollution Events), we demonstrate the use of the testbed to conduct a feasibility study of using polarization measurements in and around the O_2 *A* band for the retrieval of aerosol height information from space, as well as an to assess potential improvement in the retrieval of aerosol fine and coarse mode aerosol optical depth (AOD) through the synergic use of two future geostationary satellites, GOES-R (Geostationary Operational Environmental Satellite R-series) and TEMPO (Tropospheric Emissions: Monitoring of Pollution). Strong synergy between GEOS-R and TEMPO are found especially in their characterization of surface bi-directional reflectance, and thereby, can potentially improve the AOD retrieval to the accuracy required by GEO-CAPE.

---

[*] Corresponding author. Tel.: +1 402 472 3597.
E-mail address: jwang7@unl.edu (J. Wang).

http://dx.doi.org/10.1016/j.jqsrt.2014.03.020
0022-4073/

1. Introduction

Remote sensing of aerosols from satellite and ground-based platforms provides key datasets for understanding the role of aerosols in physical processes governing changes of air quality, visibility, surface temperature, clouds, and precipitation [1]. However, global data records of aerosol parameters have only emerged on a routine basis in the last decade, with the advent of dedicated satellite sensors placed in sun-synchronous low-earth orbits (LEOs). As seen in Table 1, these sensors include twin MODIS instruments launched in 1999 and in 2002, MISR launched in 1999, OMI and POLDER in 2004, and CALIOP in 2006. Except for CALIOP, which is an active remote sensing instrument probing the vertical distribution of aerosol backscattering, the others are all passive remote sensing instruments and are complementary to each other in their ability to characterize aerosol parameters that are commonly retrieved. Aside from the usual retrieval of aerosol optical depth (AOD), examples include the additional inversion of fine- and coarse-mode AOD ratios from MODIS' multi-spectral radiance data [2,3], derivation of non-spherical AODs and up to three size-mode AODs from MISR's multi-spectral and multi-angle radiance data [4–6], high-elevation absorbing AODs from OMI's ultraviolet (UV) radiance data [7], aerosol refractive index or single scattering albedo from POLDER's angular polarization data [8], and aerosol plume height retrieval over ocean from MERIS' reflectance data in the O_2 *A* band [9]. These examples suggest that for a full characterization of aerosol optical properties, future satellite missions should rely on a combination of multispectral and multi-angle measurements of radiance and polarization [10].

Several aerosol-related satellite missions are planned in different countries, including, for example, the Geostationary Coastal and Air Pollution Events (GEO-CAPE) and the Aerosol-Cloud-Ecosystem (ACE) missions in the USA [11], the Geostationary Environment Monitoring Spectrometer (GEMS) mission in Korea [12], and the Sentinel-4 mission (with Ocean Land Color Instrument) mission in Europe [13]. A vital question arises: how can a given sensor be optimally configured (in terms of choices of spectral wavelengths and view angles, and measured quantities such as radiances and polarization) to fulfill the mission scientific requirements, given constraints associated with the mission's budget? To address this kind of question in a cost-effective manner, a numerical testbed tool for aerosol remote sensing is highly desirable. Such a tool can provide an objective assessment of the aerosol information content resulting from any set of (planned or real) instrument configurations [14,15].

In this study, we construct such a testbed through the integrated combination of forward models for particle scattering and radiative transfer with software for inversion theory. Traditionally, two steps are required for evaluating instrument performance regarding the scientific requirements [14,15] for aerosol parameter retrieval. First, it is necessary to generate a data set of forward radiative transfer calculations for a wide-range of atmospheric and surface conditions and aerosol scattering properties, in order to simulate sensor measurements for any given configuration of solar and viewing geometry, spectral channels and desired measurement output (hereafter these simulations are called synthetic data). Second, aerosol parameters are derived from the synthetic data, potentially "degraded" by including synthetic noise, with the proposed retrieval technique, and then compared with the "true" aerosol parameters as used in synthetic data forward calculations in order to determine whether the retrieval results meet expected accuracy.

Although separate tools for both steps are currently available, efforts to integrate them in a single numerical testbed are often hindered by different aspects in retrieval algorithms developed by various research groups. These

Table 1
List of current satellite sensors with measurement specifications relevant for operational retrieval of aerosol properties.

Acronyms	Full names	Wavelengths (nm)	Measurements characteristics	References
MERIS	Medium Resolution Imaging Spectrometer	15[a] bands in 390 nm to 1040 nm including one O_2 *A* band	Radiance at single view angle	[9]
MISR	Multi-angle Imaging SpectroRadiometer	446, 558, 672, and 867 for both land and ocean algorithm	Radiance at view angles ±26.1°[b], ±45.6°, ±60.0°, and ±70.5°, and 0°	[59]
MODIS	Moderate Resolution Imaging Spectroradiometer	470, 678, 2130 for land 550, 678, 870, 1240, 1640, and 2130 for ocean	Radiance at single view angle[c]	[2,3]
OMI	Ozone Monitoring Instrument	354, 388 for Aerosol index 19 channels[d] in 332–500 for multi-channel algorithm	Radiance at single view angle	[7]
POLDER	POLarization and Directionality of the Earth's Reflectances	670, 865	Radiance and polarization at 14–16 viewing angles[e]	[8]
VIIRS	Visible Infrared Imaging Radiometer Suite	410, 440, 488, 672, 2250 nm for land 672, 746, 865, 1610, 1240, 2250 nm for ocean	Radiance at single view angle[f]	[60]
CALIOP	Cloud-Aerosol Lidar with Orthogonal Polarization	532, 1064	Layer backscattering radiance and depolarization ratio[g]	[61]

[a] 412, 442, 490, 510, 560, 620, 665, 681, 705, 753, 760, 775, 865, 890, 900 nm.

[b] Positive and negative signs respectively denote the view angles in the forward and backward plane of the local vertical (e.g., nadir view).

[c] Radiances are measured at 36 channels from 405 nm to 14395 nm.

[d] 332, 340, 343, 354, 367, 377, 388, 340, 406, 416, 426, 437, 442, 452, 463, 477, 484, 495, and 500 nm.

[e] The exact number of view angles depends on the geographical location. Radiances and linear polarization at 490 nm, 670 nm and 870 nm, and radiance-only at 440 nm, 565 nm, and 1020 nm.

[f] 22 channels with centers from 412 nm to 1201 nm.

[g] Depolarizaiton ratio is only measured at 532 nm.

aspects are hereafter called the “algorithm definition factors”; they include the pre-described aerosol single scattering properties, the wavelengths and view angles selected for the retrieval, and other assumptions regarding the properties of the Earth's surface, the aerosol vertical distribution, and the approach used for cloud-screening.

Furthermore, for the same set of real or synthetic data, some retrieval techniques may only use parts but not the entirety of the data for the retrieval. For example, POLDER measures multi-angle radiances and linear polarization at 490 nm, 670 nm and 870 nm, plus radiances at 440 nm, 565 nm, and 1020 nm, but only data at 670 nm and 870 nm are used in the operational algorithm for aerosol retrievals [8]. Consequently, the retrieved aerosol information content will depend on the sub-set of observations used in the retrieval; this makes it difficult to objectively assess the full capability of a sensor for remote sensing of aerosol properties.

To avoid the divergence of retrieval results caused by differences in algorithm definition factors other than the characteristics of measurements, a testbed for remote sensing of aerosols has to be built upon the combination of forward models with formal inversion theory that uses a standard set of variables (such as Degree of Freedom for Signal, or DFS) to quantify the retrievable information [16,17]. Since aerosol retrieval is in essence an inversion process, formal inversion theory is well suited for the full investigation of aerosol information content for any given set of synthetic or real observation data, and the comprehensive assessment of retrieval accuracy and its dependence on sources of uncertainty in model parameterizations, intrinsic model assumptions and instrument error.

However, mainly due to limitations in computational power, formal optimization theory has not been used in the satellite remote sensing of aerosols until recently [17–19]. Indeed, nearly all current operational algorithms pre-compute the radiance (and/or polarization) as a function of AOD and other aerosol properties for a wide range of Sun-satellite viewing geometries and surface reflectance values, and this synthetic data is then saved as a look-up table (LUT) [20]. The retrieval is then executed through a search procedure on the LUT, to find a set of aerosol parameters for which the corresponding pre-computed radiances (and/or polarization) best match their observed counterparts. While the LUT approach is computationally efficient, it lacks the ability to quantify the retrieval errors and to attribute error sources, and it does not offer the flexibility for a quick diagnosis of the change of retrieval performance in response to the change of algorithm definition factors. To date, errors in LUT-based retrievals are quantified merely in terms of an envelope of uncertainties, for example $0.05 \pm 0.15\tau$ for Aerosol Optical Depth (AOD or τ) retrieved from MODIS and $0.05 \pm 0.2\tau$ for MISR retrievals over land [21]. Detailed pixel-to-pixel quantification of retrieval errors has not been made – such error estimates are urgently required for assimilating these retrieved data into chemistry transport models [22–24].

To explore the variation of aerosol information content for any set of remote sensing data as a function of *a priori* constraints (or assumptions), instrument error, and algorithm definition factors, we have constructed a numerical testbed tool that combines linearized forward model calculations with optimization theory. This tool addresses several challenges that remain unanswered with the LUT approach, namely: (a) the tool will allow users to incorporate instrument errors and prior constraints in the retrieval; (b) the tool will allow users to readily change algorithm definition factors (such as selection of wavelengths and angles); (c) the tool will compute in a direct manner the sensitivity of the measured quantities (such as radiance and polarization) with respect to retrieved aerosol parameters (such as coarse/fine-mode AOD, aerosol size parameters, aerosol refractive indices, and aerosol shape factor); (d) the tool should treat the absorption spectra of trace gases in a rigorous manner; and (e) it will allow analysis of information content, degree of freedom for signal and sources of retrieval error for all desired aerosol parameters to be retrieved. While analyses using similar methods to those in feature (e) have been made in related recent work [17,18], it is feature (c) that distinguishes our tool from these two studies. This feature relies on the combination of a linearized vector radiative transfer model (VLIDORT) [30], a linearized Mie scattering code, and a linearized T-matrix code [36]. In addition, given that remote sensing of aerosols with spectroscopic data is still a largely unexplored research field [25,26], feature (d) also makes it feasible to study the effect of aerosols on the retrieval of trace gases and vice versa [27].

Components of our testbed tool are described in Section 2, and we present the model validation in Section 3. In Section 4, we demonstrate the use of this tool for the conceptual design of a retrieval algorithm to meet the requirement of GEO-CAPE for aerosols. Conclusions and discussion are in Section 5.

2. Description of the testbed

As shown in Fig. 1, the numerical testbed comprises 7 modules; they are (1) a vector linearized radiative transfer model (VLIDORT), (2) a linearized Mie scattering code, (3) a linearized T-matrix electromagnetic scattering code, (4) a surface bi-directional reflectance (BRDF) module, (5) a module that computes Rayleigh scattering and gas absorption, (6–7) two modules for the analysis, including an optimal inversion code and a visualization tool for diagnosis. Modules (1)–(5) are integrated for the forward calculation of aerosol single scattering, gas absorption and radiative transfer hereafter, and thus they together constitute the UNified Linearized Radiative Transfer Model, UNL-VRTM. Inputs for the UNL-VRTM (the forward part of the testbed) are profiles of atmospheric properties and constituents (temperature, pressure, aerosol mass concentration or layer AOD, water vapor amount and other trace gas volume mixing ratio profiles), as well as the aerosol parameters (such as size distribution and refractive index) themselves. Bearing in mind the lack of sensitivity in passive remote sensing for the retrieval of vertical profiles of aerosol properties, the UNL-VRTM as it stands now is only designed to deliver radiative calculations for a maximum of two sets of aerosol single scattering properties (e.g., aerosol size distribution, refractive index, and particle shape), typically with one fine-mode and one coarse-mode

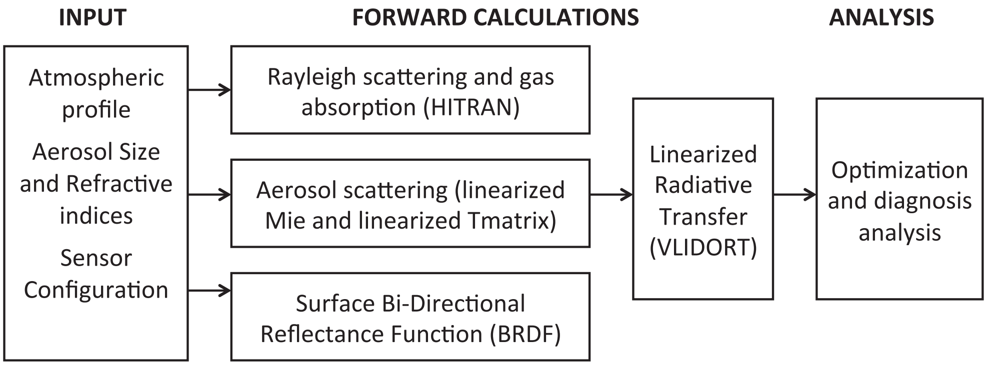

Fig. 1. Flow chart of the testbed. See text for details.

aerosol. Outputs of the testbed include synthetic data (of radiance and polarization) at user-defined wavelengths, the sensitivity of this synthetic data with respect to all aerosol particle parameters, and the information content of the synthetic data (expressed as DFS values for these physical parameters).

2.1. *Rayleigh scattering and gas absorption*

Calculation of the optical thickness (τ_R) and anisotropy factor for Rayleigh scattering follows Bodhaine et al. [28] in which the wavelength-dependent Rayleigh cross-section σ_R (cm^2 molecule^{-1}) is computed as a function of mixing ratios for N_2, O_2, H_2O, and CO_2. The phase matrix for Rayleigh scattering follows Hansen and Travis [29]; we use the set of spherical-function expansion coefficients for the phase matrix as supplied for VLIDORT [30].

Calculation of the optical thickness for gas absorption is based upon cross sections and spectroscopic line parameters in the HITRAN database [31,32] and from the literature (for O_3) [33–35]. Reference cross-sections are re-sampled to 0.01 nm resolution by spline interpolation. HITRAN provides five (in addition to the pressure shift) parameters per line that are essential to quantify the gas absorption as a function of wavelength: the line position (υ_0) in units of cm^{-1}, the intensity per absorbing molecule S (cm^{-1} cm^{-2}/molecule), the Lorentz line width parameter (α_0) in units of (cm^{-1} atm^{-1}) and its temperature dependence, and the energy of the lower state E_η (cm^{-1}). In the HITRAN database, values for α_0 and S are given for reference conditions (pressure of 1013.25 hPa and temperature of 296 K). Additional calculations are needed for temperature correction of the line intensity, and pressure-shift correction of the line position. Doppler broadening is calculated from the molecular mass and the temperature. Doppler and Lorentz broadening are included in the Voigt calculation.

2.2. *Linearized Mie/T-matrix calculation*

The calculation of aerosol single scattering parameters is made with a Linearized Mie (LMIE) scattering electromagnetic code for spherical particles and a Linearized T-matrix (LTMATRIX) scattering code for non-spherical convex and axially symmetric particles [36]. The linearized T-matrix code is based upon the T-matrix code developed by [37], but includes a linearization [36]. Common inputs for both these codes are the complex refractive index ($n_r + in_i$) and the particle size distribution (PSD) parameters for polydisperse scattering. The codes have several options to specify the PSD function: two-parameter gamma, two-parameter lognormal, three-parameter modified gamma, and four-parameter bi-lognormal. In addition, the linearized T-matrix code offers options to characterize the shape of non-spherical aerosols (spheroids, cylinders, or Chebyshev particles) [36]. For non-spherical particles, the specified size distribution is interpreted as the equivalent surface-area sphere in the linearized T-matrix calculation, regardless of the shape. Details can be found in [36].

These scattering codes compute the extinction and scattering efficiencies (Q_{ext} and Q_{sca}), the single scattering albedo (ω_A) and asymmetry parameter (g_A), and the scattering phase matrix ($\mathbf{P}_A(\Theta)$ and for expansions of $\mathbf{P}_A(\Theta)$) in terms of generalized spherical functions, the corresponding sets of expansion coefficients. The codes are linearized, in that they also generate analytic Jacobians of all these single scattering parameters with respect to input aerosol physical parameters such as n_r, n_i, PSD parameters, and the non-spherical shape factor.

2.3. *Vector linearized discrete ordinate radiative transfer (VLIDORT) model*

VLIDORT is a linearized pseudo-spherical vector discrete ordinate radiative transfer code for multiple scattering of diffuse radiation in a stratified multi-layer atmosphere. VLIDORT computes simultaneously the Stokes 4-vector parameters [I, Q, U, V] and their partial derivatives with respect to any atmospheric or surface property [30]. VLIDORT is a pure scattering model – the basic optical property inputs are the layer extinction optical depths, total single scattering albedos and scattering-matrix expansion coefficients, plus the surface reflectance.

For upwelling and downwelling radiation fields at any atmospheric level and for any viewing geometry, atmospheric -layer Jacobians are available with respect to the layer optical depths (τ_L), single scattering albedos (ω_L), and the scattering-matrix expansion coefficients. In addition, Jacobians are also available for column-integrated values of optical depth and other bulk-atmospheric properties. Jacobians can be obtained for surface properties that describe the bidirectional reflectance distribution function. The pseudo-spherical approximation is a correction for the Earth's curvature effect on solar beam attenuation; VLIDORT also has the delta-M approximation for dealing with sharply-peaked forward scattering.

Computation of the Stokes vector in VLIDORT requires input of an optical property set $[\tau_L,\ \omega_L,\ \langle \mathbf{B}_L^j \rangle_{j=0,\,J}]$ for each atmospheric layer where $\langle\ \rangle_{j=0,\ j}$ denotes the vector that consists of elements having the similar expression as that inside $\langle\ \rangle$ but for $j=0$, J. For each atmospheric layer L, the optical property inputs are assumed constant and are given by

$$\tau_L = \tau_G + \tau_R + \tau_A \tag{1}$$

$$\omega_L = \frac{\omega_A \tau_A + \tau_R}{\tau_L} \tag{2}$$

$$\mathbf{B}_L^j = \frac{\omega_A \tau_A \mathbf{B}_A^j + \tau_R \mathbf{B}_R^j}{\omega_A \tau_A + \tau_R} \tag{3}$$

where τ_G, τ_R, and τ_A are the optical depths for gas absorption, Rayleigh scattering, and aerosol extinction, respectively; ω_A is the aerosol single scattering albedo; $\mathbf{B}_A^j$ and $\mathbf{B}_R^j$ are 4×4 matrices of expansion coefficients for aerosol and Rayleigh scattering. Note that, for Rayleigh scattering, $\mathbf{B}_R^j = \mathbf{0}$ when $j \geq 3$.

Since VLIDORT generates Jacobians with respect to layer-integrated single scattering properties in each atmospheric layer as well as column-integrated single scattering property as a whole, and LMIE and LTMATRIX offer the sensitivity of aerosol scattering properties to microphysical aerosol physical parameters, an integrated use of VLIDORT and LTMATRIX/LMIE can, in principle, provide the Jacobians of Stokes parameters with respect to both aerosol single scattering properties as well as aerosol microphysical parameters (e.g., refractive index, size, and shape). Practically, the VLIDORT calculation of Jacobians of any Stokes parameter ξ with respect to any aerosol parameter x proceeds according to

$$\begin{aligned} x\frac{\partial \xi}{\partial x} &= x\left[\frac{\partial \xi}{\partial \tau_L}\quad \frac{\partial \xi}{\partial \omega_L}\quad \left\langle \frac{\partial \xi}{\partial \mathbf{B}_L^j} \right\rangle_{j=0,\,J}\right]\left[\frac{\partial \tau_L}{\partial x}\quad \frac{\partial \omega_L}{\partial x}\quad \left\langle \frac{\partial \mathbf{B}_L^j}{\partial x} \right\rangle_{j=0,J}\right]^T \\ &= \left[\tau_L\frac{\partial \xi}{\partial \tau_L}\quad \omega_L\frac{\partial \xi}{\partial \omega_L}\quad \left\langle \mathbf{B}_L^j\frac{\partial \xi}{\partial \mathbf{B}_L^j} \right\rangle_{j=0,J}\right][\phi_x,\ \ \varphi_x,\ \ \left\langle \mathbf{\Psi}_x^j \right\rangle_{j=0,J}]^T. \end{aligned} \tag{4}$$

The first square bracket on the right-hand side of Eq. (4) contains quantities computed internally by VLIDORT, while the second so-called "transformation vector" must be supplied by users and is defined as

$$\phi_x = \frac{x}{\tau_L}\frac{\partial \tau_L}{\partial x};\quad \varphi_x = \frac{x}{\omega_L}\frac{\partial \omega_L}{\partial x};\quad \mathbf{\Psi}_x^j = \frac{x}{\mathbf{B}_L^j}\frac{\partial \mathbf{B}_L^j}{\partial x}. \tag{5}$$

This transformation vector can be further expanded as

$$[\phi_x,\ \ \varphi_x,\ \ \left\langle \mathbf{\Psi}_x^j \right\rangle_{j=0,J}]^T = \mathbf{\Pi}[\phi'_x,\ \ \varphi'_x,\ \ \left\langle \mathbf{\Psi}_x^{\prime j} \right\rangle_{j=0,J}]^T \tag{6}$$

Where $\left[\phi'_x,\ \ \varphi'_x,\ \ \left\langle \mathbf{\Psi}_x^{\prime j} \right\rangle_{j=0,J}\right] = \left[x\frac{\partial \tau_A}{\partial x},\quad x\frac{\partial \delta_A}{\partial x},\quad \left\langle x\frac{\partial \mathbf{B}_A^j}{\partial x} \right\rangle_{j=0,J}\right]^T$,

and $\mathbf{\Pi}$ is a matrix expressed by

$$\mathbf{\Pi} = \begin{bmatrix} \frac{1}{\tau_L} & 0 & \mathbf{0} \\ -\frac{1}{\tau_L} & \frac{1}{\delta_A+\delta_R} & \mathbf{0} \\ \mathbf{0} & \left\langle \frac{\mathbf{B}_A^j - \mathbf{B}_R^j}{\mathbf{B}_L^j(\delta_A+\delta_R)} \right\rangle_{j=0,J} & \left\langle \frac{\delta_A}{\mathbf{B}_L^j(\delta_A+\delta_R)} \right\rangle_{j=0,J} \end{bmatrix}. \tag{7}$$

Here, δ_A is the scattering optical depth of aerosols. The detailed derivations of the matrix $\mathbf{\Pi}$ are presented in Appendix A. Hence, the transformation vector for calculating Stokes profile Jacobians with respect to τ_A, ω_A, and $\mathbf{B}_A^j$ can be obtained by combining Eqs. (6) and (7), and the components of this vector are listed in Table 2.

In an atmosphere where both fine (superscript "s") and coarse (superscript "c") aerosol particles co-exist, the ensemble aerosol optical properties may be derived by assuming external mixing:

$$\begin{cases} \tau_A = \tau_A^s + \tau_A^c \\ \delta_A = \delta_A^s + \delta_A^c \\ \mathbf{B}_A^j = \frac{\delta_A^s \mathbf{B}_A^{s\ j} + \delta_A^c \mathbf{B}_A^{c\ j}}{\delta_A^s + \delta_A^c} \end{cases} \tag{8}$$

We can generate the transformation vectors (Table 3) for any of the following parameters τ_A^s, ω_A^s, m_A^s, n_i^s, n_r^s, σ_g^s, r_g^s, ε^s, H^s, and τ_A^c, ω_A^c, m_A^c, n_i^c, n_r^c, σ_g^c, r_g^c, ε^c, and H^c, where σ_g, r_g, and H denote respectively the median and geometric standard deviation of particle radius (e.g., two parameters in the log-normal aerosol number distribution), and the scale height of aerosol extinction; m_A *is* the aerosol mass concentration and ε the shape factor of the non-spherical particle. Details of the algebra for deriving the transformation vectors may be found in Appendix A. Note that the shape of the aerosol extinction vertical profile in the testbed is assumed to be constant or exponentially decreasing with height or quasi-Gaussian (Appendix A); in the main text, we use the exponential form. The analytical formulas for ϕ'_x, φ'_x, and $\mathbf{\Psi}_x^{\prime j}$ for coarse mode aerosol parameters are the same as their counterparts for fine-mode aerosols; we need only replace superscript "s" with "c" in Table 3 entries. Jacobians with respect to the fine mode fraction, either in terms of AOD (f_τ) or in terms of the mass concentration (f_m), can be derived from the corresponding Jacobians with respect to modal AOD and

Table 2
Elements of transformation vector for various aerosol single scattering parameters (composite of fine and coarse mode).

x	ϕ_x	φ_x	$\mathbf{\Psi}_x^j$
τ_A	$\frac{\tau_A}{\tau_L}$	$\frac{\tau_A}{\tau_L}\left(\frac{\omega_A}{\omega_L}-1\right)$	$\begin{cases} \frac{\omega_A\tau_A}{\omega_L\tau_L}\left(\frac{\mathbf{B}_A^j}{\mathbf{B}_L^j}-1\right) & for\ j<3 \\ \frac{\tau_R}{\omega_L\tau_L} & for\ j\geq3 \end{cases}$
ω_A	0	$\frac{\omega_A\tau_A}{\tau_L\omega_A\tau_A+\tau_R}$	Same as above
B_A^j	0	0	$\begin{cases} \frac{\omega_A\tau_A\mathbf{B}_A^j}{\omega_A\tau_A\mathbf{B}_A^j+\tau_R\mathbf{B}_R^j} & for\ \ m=j<3 \\ 1 & for\ \ m=j\geq3 \\ 1 & for\ \ m\neq j \end{cases}$

Table 3
Elements of transformation vector for various microphysical parameters of fine and coarse mode aerosols[a].

x	ϕ'_{x^s}	φ'_{x^s}	$\boldsymbol{\Psi}'^{j}_{x^s}$
$\tau_{\mathrm{A}}^{\mathrm{s}}$	$\tau_{\mathrm{A}}^{\mathrm{s}}$	$\delta_{\mathrm{A}}^{\mathrm{s}}$	$\frac{\delta_{\mathrm{A}}^{\mathrm{s}}}{\tau_{\mathrm{A}}}(\mathbf{B}_{\mathrm{A}}^{\mathrm{s}\,j}-\mathbf{B}_{\mathrm{A}}^{j})$
$\omega_{\mathrm{A}}^{\mathrm{s}}$	0	$\delta_{\mathrm{A}}^{\mathrm{s}}$	$\frac{\delta_{\mathrm{A}}^{\mathrm{s}}}{\tau_{\mathrm{A}}}(\mathbf{B}_{\mathrm{A}}^{\mathrm{s}\,j}-\mathbf{B}_{\mathrm{A}}^{j})$
$m_{\mathrm{A}}^{\mathrm{s}}$	$m_{\mathrm{A}}^{\mathrm{s}}\frac{3}{4}\frac{Q_{\mathrm{ext}}^{\mathrm{s}}}{\rho_{\mathrm{A}}^{\mathrm{s}}\,r_{\mathrm{eff}}^{\mathrm{s}}}$	$m_{\mathrm{A}}^{\mathrm{s}}\frac{3}{4}\frac{Q_{\mathrm{sca}}^{\mathrm{s}}}{\rho_{\mathrm{A}}^{\mathrm{s}}\,r_{\mathrm{eff}}^{\mathrm{s}}}$	$\frac{\delta_{\mathrm{A}}^{\mathrm{s}}}{\tau_{\mathrm{A}}}(\mathbf{B}_{\mathrm{A}}^{\mathrm{s}\,j}-\mathbf{B}_{\mathrm{A}}^{j})$
$n_{\mathrm{r}}^{\mathrm{s}},\ n_{\mathrm{i}}^{\mathrm{s}},$	$\tau_{\mathrm{A}}^{\mathrm{s}}\frac{x^{\mathrm{s}}}{Q_{\mathrm{ext}}^{\mathrm{s}}}\frac{\partial Q_{\mathrm{ext}}^{\mathrm{s}}}{\partial x^{\mathrm{s}}}$	$\delta_{\mathrm{A}}^{\mathrm{s}}\frac{x^{\mathrm{s}}}{Q_{\mathrm{sca}}^{\mathrm{s}}}\frac{\partial Q_{\mathrm{sca}}^{\mathrm{s}}}{\partial x^{\mathrm{s}}}$	$\frac{1}{\delta_{\mathrm{A}}^{\mathrm{s}}}(\varphi'_{x^s}\mathbf{B}_{\mathrm{A}}^{\mathrm{s}\,j}-\varphi'_{x^s}\mathbf{B}_{\mathrm{A}}^{j})+x^{\mathrm{s}}\frac{\partial\mathbf{B}_{\mathrm{A}}^{\mathrm{s}\,j}}{\partial x}$
$r_{\mathrm{g}}^{\mathrm{s}},\ \sigma_{\mathrm{g}}^{\mathrm{s}},\ \varepsilon^{\mathrm{s}}$	$\tau_{\mathrm{A}}^{\mathrm{s}}\left(\frac{x^{\mathrm{s}}}{Q_{\mathrm{ext}}^{\mathrm{s}}}\frac{\partial Q_{\mathrm{ext}}^{\mathrm{s}}}{\partial x^{\mathrm{s}}}-\frac{x^{\mathrm{s}}}{r_{\mathrm{eff}}^{\mathrm{s}}}\frac{\partial r_{\mathrm{eff}}^{\mathrm{s}}}{\partial x^{\mathrm{s}}}\right)$	$\delta_{\mathrm{A}}^{\mathrm{s}}\left(\frac{x^{\mathrm{s}}}{Q_{\mathrm{sca}}^{\mathrm{s}}}\frac{\partial Q_{\mathrm{sca}}^{\mathrm{s}}}{\partial x^{\mathrm{s}}}-\frac{x^{\mathrm{s}}}{r_{\mathrm{eff}}^{\mathrm{s}}}\frac{\partial r_{\mathrm{eff}}^{\mathrm{s}}}{\partial x^{\mathrm{s}}}\right)$	$\frac{1}{\delta_{\mathrm{A}}^{\mathrm{s}}}(\varphi'_{x^s}\mathbf{B}_{\mathrm{A}}^{\mathrm{s}\,j}-\varphi'_{x^s}\mathbf{B}_{\mathrm{A}}^{j})+x^{\mathrm{s}}\frac{\partial\mathbf{B}_{\mathrm{A}}^{\mathrm{s}\,j}}{\partial x}$
H^{s}	$H^{\mathrm{s}}\frac{\partial\tau_{\mathrm{A}}^{\mathrm{s}}}{\partial h^{\mathrm{s}}}$	$\phi'_x\ \omega_{\mathrm{A}}^{\mathrm{s}}$	$\frac{\delta_{\mathrm{A}}^{\mathrm{s}}}{\delta_{\mathrm{A}}}(\mathbf{B}_{\mathrm{A}}^{\mathrm{s}\,j}-\mathbf{B}_{\mathrm{A}}^{j})$

[a] Expressions are shown only for fine-mode parameters (x^{s}); expressions for coarse mode parameters are the same but with superscript s replaced by c.

mass, respectively:

$$f_\tau\frac{\partial\xi}{\partial f_\tau}=\tau_{\mathrm{A}}^{\mathrm{s}}\frac{\partial\xi}{\partial\tau_{\mathrm{A}}^{\mathrm{s}}}-\frac{f_\tau}{1-f_\tau}\tau_{\mathrm{A}}^{\mathrm{c}}\frac{\partial\xi}{\partial\tau_{\mathrm{A}}^{\mathrm{c}}} \tag{9}$$

$$f_m\frac{\partial\xi}{\partial f_m}=m_{\mathrm{A}}^{\mathrm{s}}\frac{\partial\xi}{\partial m_{\mathrm{A}}^{\mathrm{s}}}-\frac{f_m}{1-f_m}m_{\mathrm{A}}^{\mathrm{c}}\frac{\partial\xi}{\partial m_{\mathrm{A}}^{\mathrm{c}}} \tag{10}$$

Details of these necessary VLIDORT inputs are presented in Appendix A.

2.4. Surface BRDF model

VLIDORT has a supplementary module for specification of the surface BRDF as a linear combination of (up to) three semi-empirical kernel functions; for details, see [30]. This supplementary module can also provide partial derivatives of the BRDF with respect to the kernel weighting factors or with respect to kernel parameters such as the wind speed for glitter reflectance. These kernel functions include Lambertian, Ross-Thick, and Li-Sparse functions [38,39], a Bi-directional Polarization Distribution Function [40], and an ocean surface model based on the Cox-Munk model [65]. In addition, VLIDORT has an option for using a surface-leaving radiation field, either as a fluorescence term or as a water-leaving term expressed as a function of chlorophyll absorption.

2.5. Optimization retrieval

Our approach is based upon non-linear optimal estimation theory [16,41], and is similar to that of Waquet et al. [18] as applied to the Aerosol Polarimetry Sensor (APS) aerosol algorithm, and Hasekamp and Landgraf [42] for the GOME-2 aerosol retrieval algorithm. The principal aim is to retrieve an optimal set of aerosol parameters from a combination of satellite measurements of radiance/polarization, and *a priori* knowledge of this set of aerosol parameters [43,44]. The retrieval proceeds by simultaneously and iteratively minimizing the cost function ϕ which is the sum of two L^2-norm functionals, the first expressing differences between observations and simulations constrained by the total measurement error covariance matrix ($\mathbf{E}_{\mathrm{T}}$) and the second expressing differences between retrieved ($\mathbf{x}$) and *a priori* ($\mathbf{x}_{\mathrm{a}}$) state vectors constrained through the *a priori* covariance matrix ($\mathbf{E}_{\mathrm{a}}$). The cost function is

$$\Phi=\|\mathbf{E}_{\mathrm{T}}^{-(1/2)}\{\mathbf{K}_i(\mathbf{x}_{i+1}-\mathbf{x}_i)-[\mathbf{y}-\mathbf{F}(\mathbf{x}_i)]\}\|^2+\|\mathbf{E}_{\mathrm{a}}^{-(1/2)}(\mathbf{x}_{i+1}-\mathbf{x}_{\mathrm{a}})\|^2 \tag{11}$$

here, $\mathbf{y}$ is the measurement vector, $\mathbf{F}$ is the forward model (UNL-VRTM) that combines components described in Sections 2.1–2.4, $\mathbf{E_T}$ is the total error covariance matrix, and $\mathbf{x}_{i+1}$ and $\mathbf{x}_i$ are the retrieval state vectors for the current and previous iterations, respectively. $\mathbf{x}_{\mathrm{a}}$ is the *a priori* state vector, and $\mathbf{E_a}$ is the *a priori* error covariance matrix. $\mathbf{K}_{\mathrm{i}}$ is the Jacobian or weighting function matrix at iteration step i, defined as $\partial\mathbf{F}/\partial\mathbf{x}_i$, which is essentially the matrix of sensitivity functions of Stokes parameters (ξ) with respect to any of the parameters to be retrieved (e.g., $x(\partial\xi/\partial x)$). Here, the retrieval state vector ($\mathbf{x}$) consists of the following 15 elements: $\tau_{\mathrm{A}}, f_\tau$, $\mathrm{n}_{\mathrm{i}}^{\mathrm{s}}$, $n_{\mathrm{i}}^{\mathrm{s}}$, $n_{\mathrm{r}}^{\mathrm{s}}$, $\sigma_{\mathrm{g}}^{\mathrm{s}}$, $r_{\mathrm{g}}^{\mathrm{s}}$, ε^{s}, H^{s} and $n_{\mathrm{i}}^{\mathrm{c}}$, $n_{\mathrm{r}}^{\mathrm{c}}$, $\sigma_{\mathrm{g}}^{\mathrm{c}}$, $r_{\mathrm{g}}^{\mathrm{c}}$, ε^{c}, and H^{c}. Note, here f_τ and H denote the fraction of AOD in fine mode and scale height respectively.

The first term on the right-hand side of Eq. (11) is the weighted least square error functional that represents the distance between the measured and modeled quantities. For simplicity, the total error covariance matrix is assumed zero-off-diagonal, which means that errors in each individual measurement are independent. The diagonal values are thus error variances for individual measurements, comprising random Gaussian instrumental errors and forward model errors. The instrumental error includes the contributions from instrument noise and calibration error. The forward model error includes errors in the simulated radiances propagated from uncertainties in assumed parameterizations of atmospheric and surface properties (for example gas absorption cross-sections), and errors due to mathematical and physical assumptions in the forward model itself (for example truncation errors in the phase matrix).

The optimal *a posteriori* solution is given by Rodgers [41]

$$\mathbf{x}_{i+1}=\mathbf{x}_i+(\mathbf{K}_i^T\mathbf{E}_{\mathrm{T}}^{-1}\mathbf{K}_i+\mathbf{E}_a^{-1})^{-1}\{\mathbf{K}_i^T\mathbf{E}_{\mathrm{T}}^{-1}[\mathbf{y}-\mathbf{F}(\mathbf{x_i})]-\mathbf{E}_{\mathrm{a}}^{-1}(\mathbf{x}_{i+1}-\mathbf{x_a})\} \tag{12}$$

The superscript T here means transpose of the matrix. From optimal estimation theory, the solution (*a posteriori*) error covariance matrix for the retrieved parameters is

$$\hat{\mathbf{E}} = (\mathbf{E}_{\mathrm{a}}^{-1} + \mathbf{K}_i^T \mathbf{E}_{\mathrm{T}}^{-1} \mathbf{K}_i)^{-1} \qquad (13)$$

Errors in derived variables (e.g., $\tau_{\mathrm{A}}^{\mathrm{s}}$) can be determined from the errors of the retrieved parameters and the Jacobians of these derived variables with respect to the retrieval elements. For the purpose of quantifying information contained in the observation, only the error covariance and Jacobian matrix, and not the retrieval, are important. To obtain the link between the retrieval to the true state, we differentiate Eq. (12) and assume a linear forward model in the vicinity of the true state:

$$\mathbf{A} = \frac{\partial \mathbf{x}_{i+1}}{\partial \mathbf{x}} = (\mathbf{E}_{\mathrm{a}}^{-1} + \mathbf{K}_i^T \mathbf{E}_{\mathrm{T}}^{-1} \mathbf{K}_i)^{-1} \mathbf{K}_i^T \mathbf{E}_{\mathrm{T}}^{-1} \mathbf{K}_i \qquad (14)$$

A is called the averaging kernel matrix, which quantifies the ability of the retrieval to infer a *posteriori* state vector ($\hat{\mathbf{x}}$) given the relationship between **y** and **x** at

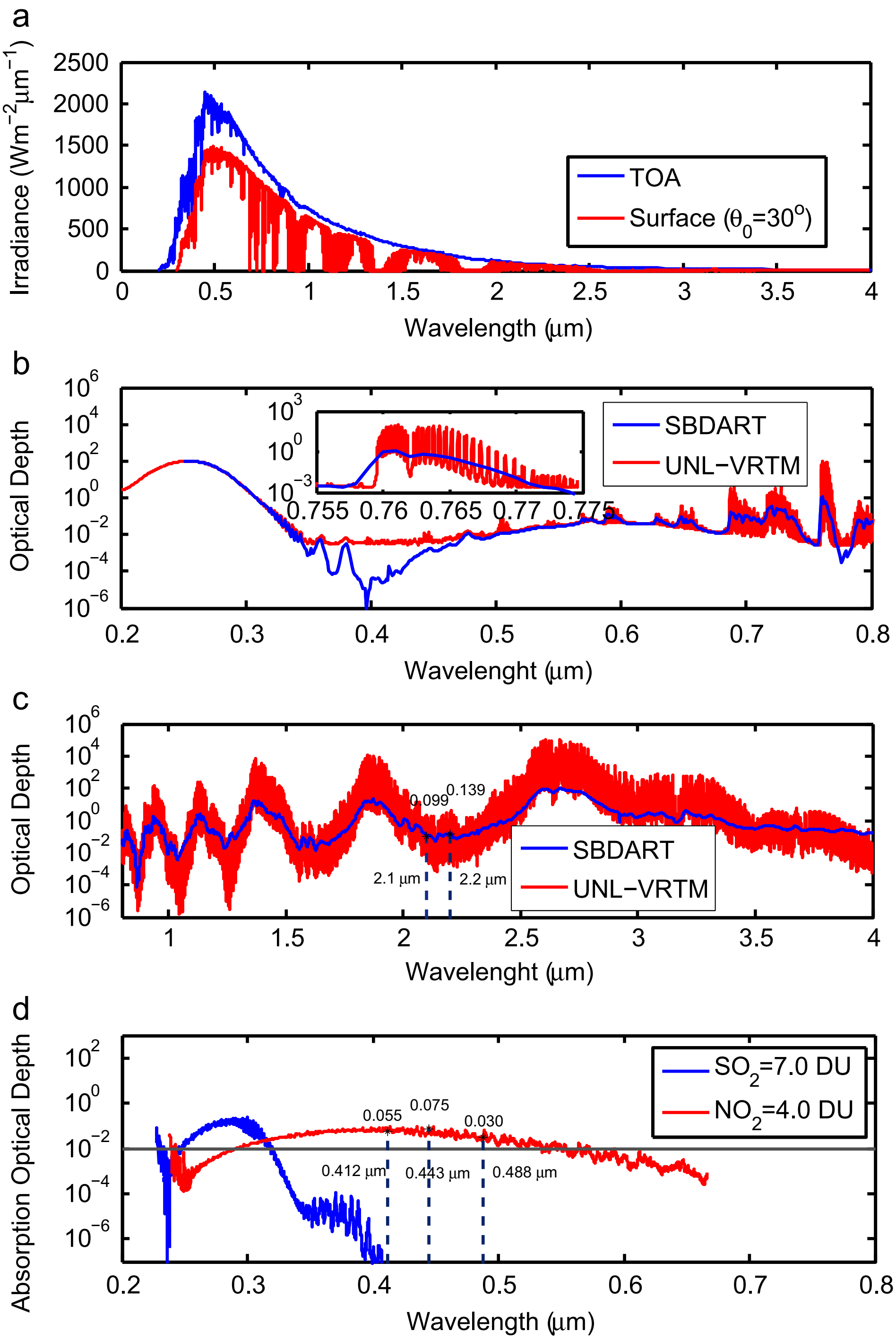

Fig. 2. (a) Downward solar spectral irradiance at the TOA and the surface for solar zenith angle of 30°. (b) Total-atmosphere gas absorption optical depth in the range 0.2–0.8 μm. (c) Same as (b) but for 0.8–4 μm. (d) Optical depth of SO_2 and NO_2 in polluted cases. Also shown in (b) and (c) are the optical depth computed from Santa Barbara DISORT Atmospheric Radiative Transfer (SBDART) model [45]. The mid-latitude summer atmospheric profile is assumed (McClatchey et al. [62]).

the linearization point (i.e., **K**) for specified observation noise and a *priori* characterization. Thus, a perfect retrieval results in the identity matrix for **A**, while a null matrix for **A** indicates that no information can be gained from the observation. The trace of **A** is the Degree of Freedom for Signal, DFS = Trace(**A**), which is a measure of the number of independent pieces of information that can be gleaned from the retrieval. Note, in reality $\mathbf{E}_a$ and $\mathbf{K}_i$ can be connected. For example, in the extreme case when $\mathbf{E_a}$ is approaching infinite, it also means that $\mathbf{K}_i$ is approaching zero, i.e., the instrument has no information for the retrieval parameter; hence, in this case, DFS is approaching zero.

3. Forward model examples and benchmarking

Fig. 2a shows the downward solar spectral irradiance at the top-of-atmosphere and at the surface for a solar zenith angle of 30°. Spectral regions dominated by gas absorption can be clearly identified, including the O_3 Hartley-Huggins bands in the UV, the O_2 *B* band (0.69 μm) and O_2 *A* band (0.76 μm), as well as a number of water vapor bands. The spectroscopic calculations shown in Fig. 2 were performed at a resolution of 0.01 nm. In general this resolution is high enough to pick up fine structure in gas absorptions. In the UV below 300 nm, and in parts of the O_2 *A* and O_2 *B* bands, whole-atmosphere gas absorption optical depths can reach 50 or more, and the downward irradiance is nearly zero at the ground (Fig. 2b). The inset in Fig. 2b shows a close-up view of the fine structure in absorption optical depth for the O_2 *A* band, with dual peaks centered at 0.761 μm and 0.764 μm, and a deep, narrow valley around 0.762 μm. Similarly, the continuum of water vapor absorption from the near-infrared to ~4 μm is also well simulated (Fig. 2c). Also of note is the non-negligible absorption of SO_2 and NO_2 in UV and blue wavelength regions

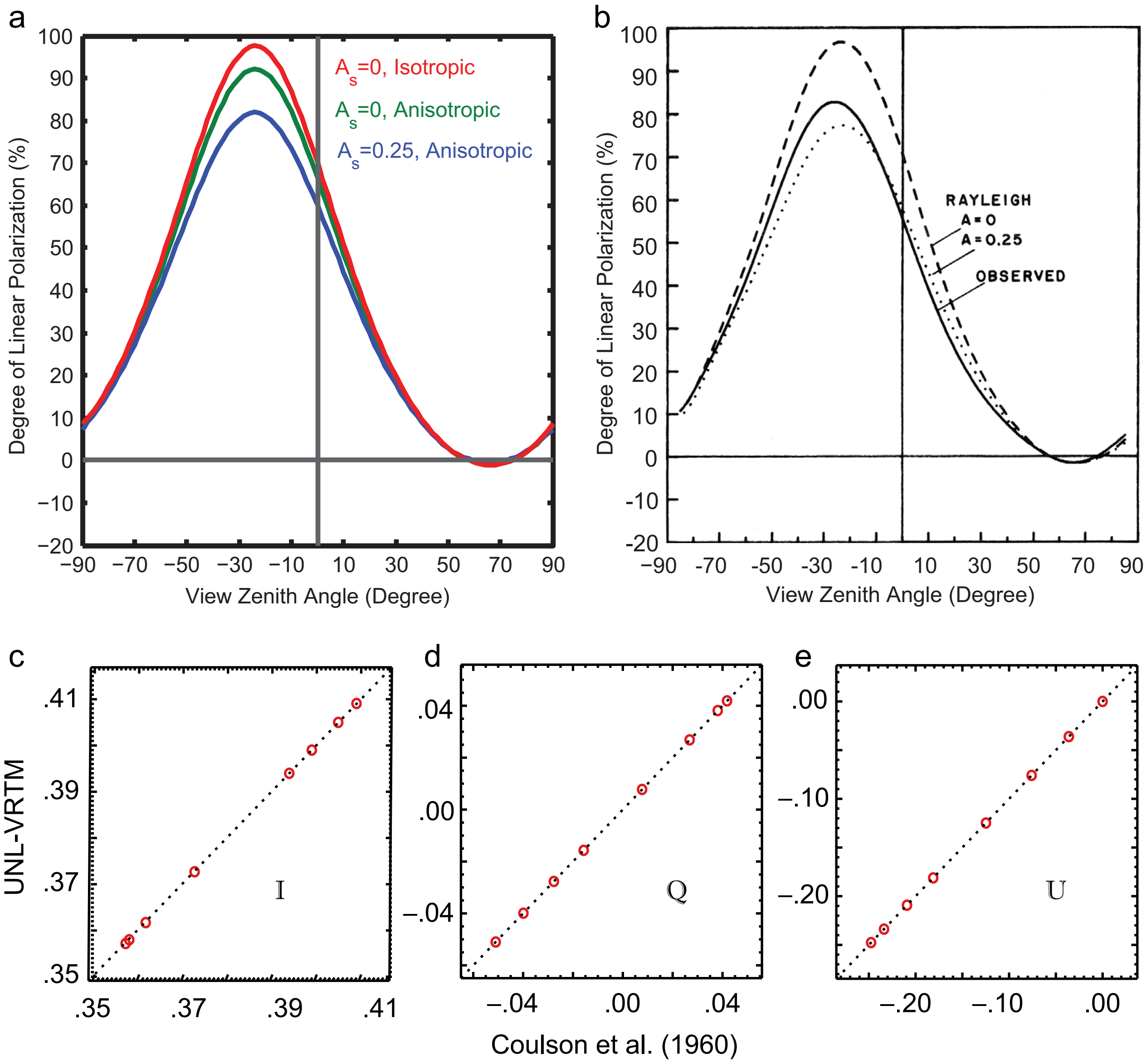

Fig. 3. Degree of linear polarization ($-Q/I$) of downward radiation for a pure Rayleigh atmosphere: (a) computed by UNL-VRTM for the case analyzed in Figure 5.7 of Coulson [46] and shown here as (b). (c)–(e) shows the comparisons of *I*, *Q*, and *U* computed by Coulson et al. [47] and those from UNL-VRTM. In (a) and (b), A_s represents the surface albedo value. In (c) and (d), the calculation is for $\tau=1.0$, surface albedo $\rho=0.25$, $\cos\theta_0=0.8$, and for 8 different viewing angles values. See details in the text.

respectively (Fig. 2d). In urban regions, high SO_2 and NO_2 can together contribute optical depths of around 0.03–0.07 (Fig. 2d). Hence, in order to take advantage of low surface reflectance in the UV and the use of deep-blue wavelengths for the retrieval of AOD in urban regions, it is critical to treat absorption by SO_2 and NO_2. In contrast, calculations performed at moderate spectral resolution (such as those from Santa Barbara Discrete-Ordinate Atmospheric Radiative Transfer, or SBDART [45], shown as the blue lines in Figs. 2b and c) do not resolve fine-structure details, sometimes missing the absorption lines for SO_2 or NO_2, and in general producing significant underestimation of optical depths in the O_2 *A* band.

Fig. 3 shows the calculation of the degree of linear polarization (DOLP) of downward radiation in a pure Rayleigh scattering atmosphere. The solid blue line in Fig. 3a (dotted line in Fig. 3b) reproduces the theoretical results shown in Figure 5.7 of Coulson's 1988 book [46], which was used to interpret the DOLP measured at Mauna Loa Observatory on February 19, 1977. Furthermore, Fig. 3a shows that the anisotropy in Rayleigh scattering reduces the peak DOLP by 5% (e.g., the difference between the green and red lines) at 0.7 μm. Surface reflection and its concomitant increase of atmosphere scattering will decrease the DOLP of downward radiation. An increase of surface reflectance from 0 to 0.25 decreases the peak DOLP by 10%.

Quantitatively, the Stokes-vector *I*, *Q*, and *U* components computed with UNL-VRTM differ from their counterparts found in the tables by Coulson et al. [47] by average (relative) deviations of 1.9×10^{-4} (0.05%), 2×10^{-5} (0.14%), and 4×10^{-5} (0.03%), respectively (Figs. 3c–e). These differences are similar to the values 2.1×10^{-4}, 9×10^{-5}, and 7×10^{-5} identified by Evans and Stephens [48]. More recently, Rayleigh-atmosphere benchmark results have been re-computed by Natraj and Hovenier [49] to a much higher degree of accuracy; this work also included benchmarking of the VLIDORT model.

Fig. 4 shows benchmark calculations of four Stokes parameters for radiative transfer in an aerosol-only atmosphere. Garcia and Siewert [50] documented their results for unpolarized incident radiation at 951 nm and solar zenith angle cosine 0.2, for an atmosphere with a Lambertian reflectance of 0.1. The aerosols in that atmosphere were assumed to satisfy a gamma-function size distribution with $r_{eff}=0.2$ μm and $v_{eff}=0.07$ μm, and a refractive index yielding an aerosol single scattering albedo of 0.99. Compared to their results, the Stokes four parameters computed

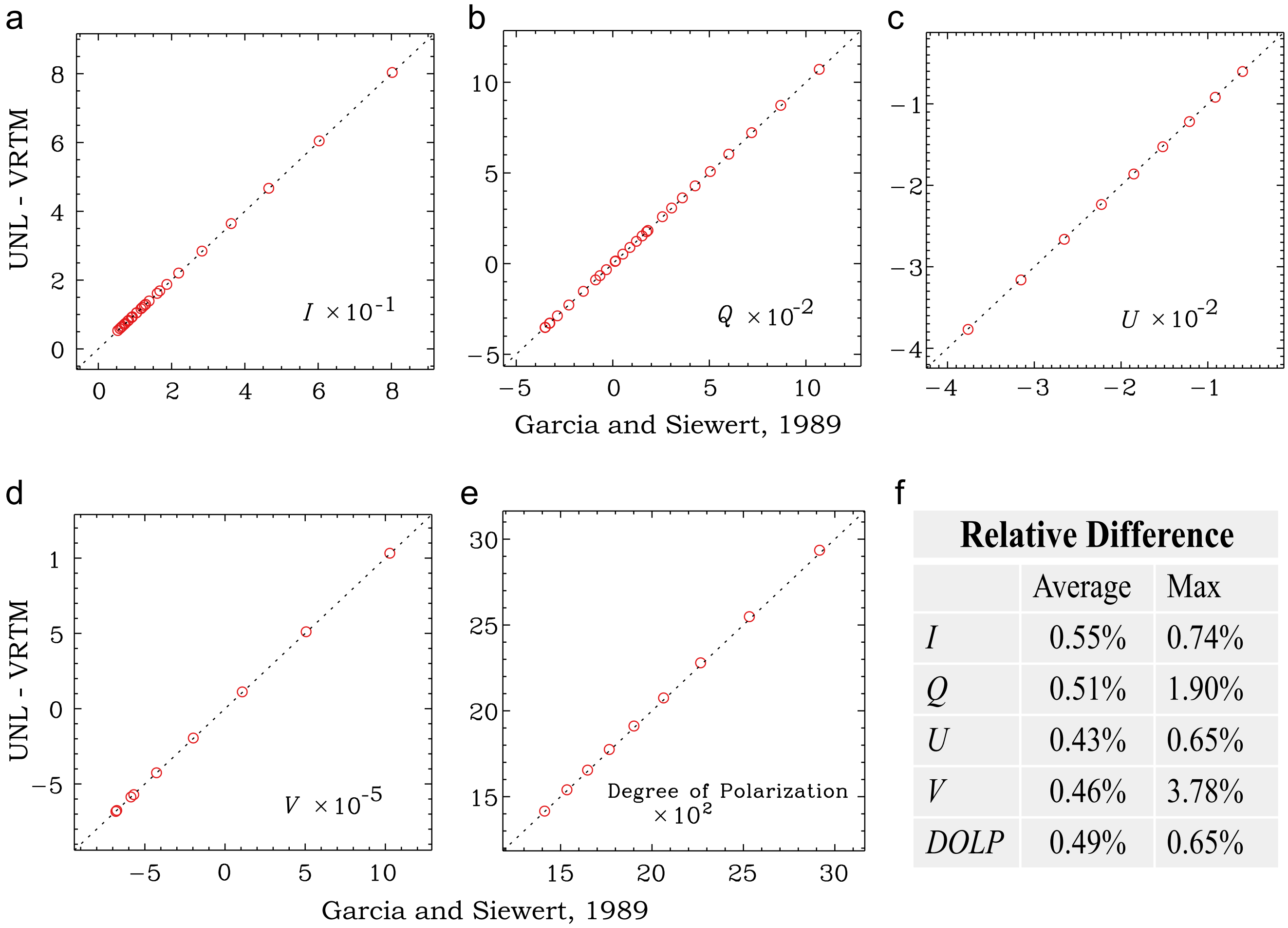

Relative Difference		
	Average	Max
I	0.55%	0.74%
Q	0.51%	1.90%
U	0.43%	0.65%
V	0.46%	3.78%
DOLP	0.49%	0.65%

Fig. 4. Counterparts in Tables 3–10 of Garcia and Siewert [50] for upwelling radiation on the top of the same atmospheric conditions of aerosol scattering. No gas absorption and Rayleigh scattering are considered. Note that compared here are *I* and *Q* values reported in Ref. [50] for 9 view angles (with cosine values from 0.1 to 0.9 at equal spacing of 0.1) and 3 relative azimuth angles (0, $\pi/2$, and π), which yields a total of 27 data points. For *U* and *V*, their values are reported for the same 9 viewing angles but for one relative azimuth angle ($\pi/2$) only. See details in the text. The calculation is performed at 951 nm for AOD = 1.0, and aerosol size distribution parameters $r_{\mathrm{eff}}=0.2$, and $v_{\mathrm{eff}}=0.07$, refractive index = 1.44, and single scattering albedo 0.99 [50].

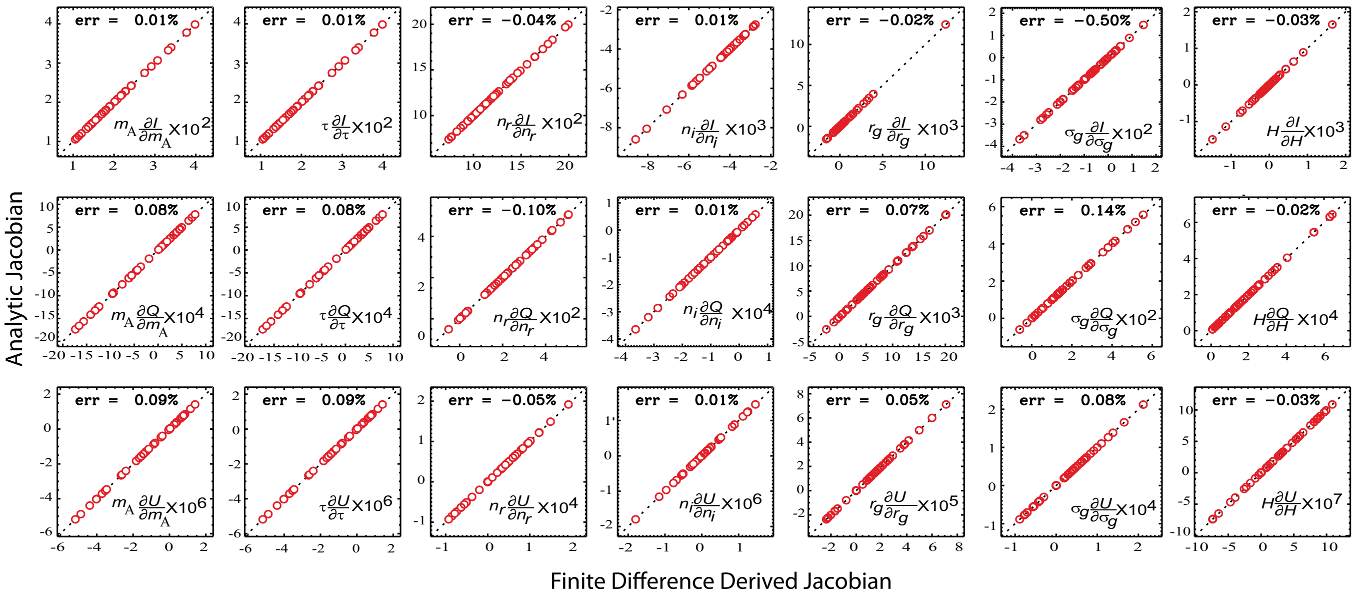

Fig. 5. Intercomparison of Jacobians ($\partial\xi/\partial \ln x$) calculated with UNL-VRTM using the analytical method (y-axis) with those computed from UNL-VRTM using finite difference estimates (x-axis). Here S is one of the Stokes parameters: I (top row), Q (middle row), and U (last row). x is one of 7 parameters associated with fine-mode aerosols - these parameters are the mass M (first column from the right), optical depth τ (2nd column), real part m_r (3rd column) and imaginary part m_i (4th column) of the refractive index, geometric radius r_g (5th column) and geometric standard deviation σ_g (6th column) of the lognormal size distribution, as well as the aerosol peak height H (7th column). Note, the calculation is done for an atmosphere containing both fine (sulfate) and coarse (dust) mode aerosols as described in Hess et al.[63].

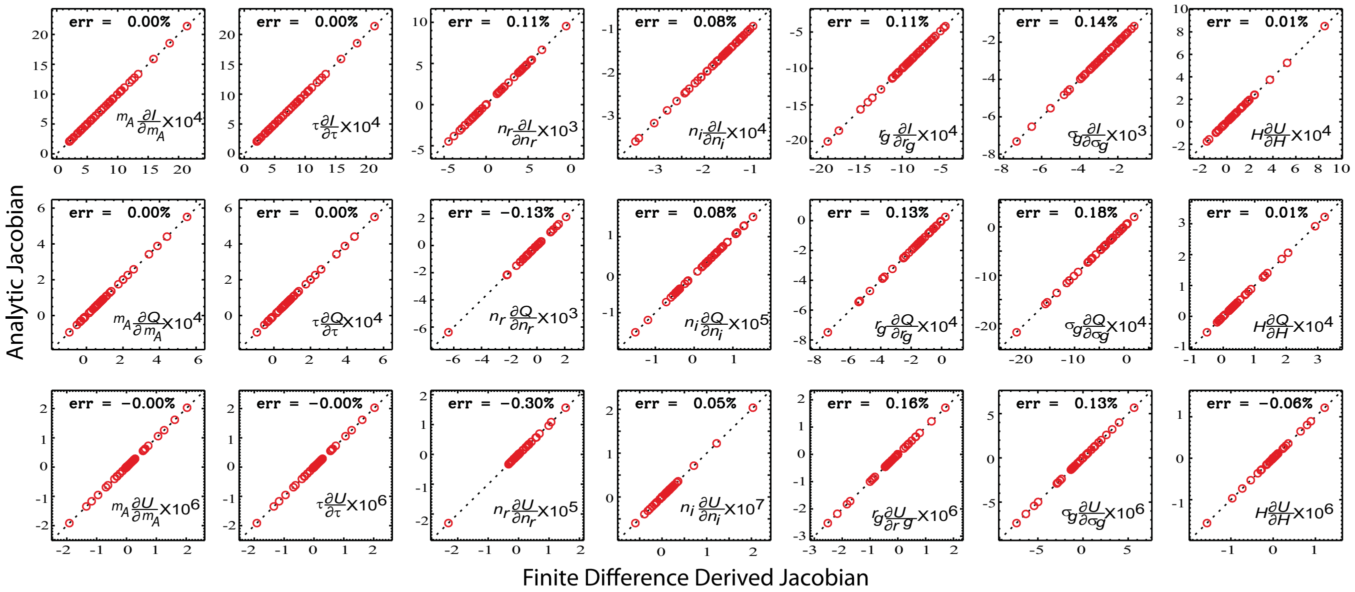

Fig. 6. Same as in Fig. 5, but for coarse mode aerosols.

by UNL-VRTM show relative differences of less than 0.6%, with maximum relative differences (at certain viewing geometries) of up to 2% for Q and 3.8% for V. The DOLP computed from the UNL-VRTM (with 15 streams for the hemisphere) and documented by Garcia and Siewert [50] (with 3 streams) differ on average by 0.5%, with a maximum relative difference of 0.65%.

The simultaneous calculation of analytic Jacobians of the four Stokes parameters with respect to the aerosol optical depth, size parameters, refractive indices, and aerosol-loading peak height for both fine and coarse model aerosols may be validated against Jacobians calculated using the finite difference method (Figs. 5 and 6). Overall, results from the two methods are highly correlated as seen in the scatter plots shown in Figs. 5 and 6. Relative differences in all comparisons are less than 0.5%, and in many cases the differences are less than 0.05%.

4. Case demonstration for GEO-CAPE

4.1. Polarization sensitivity in O_2 A band to aerosol vertical profile

One of the requirements in the GEO-CAPE science traceability matrix is to retrieve the aerosol centroid height (the altitude where maximum extinction occurs) from passive remote sensing [51]. This requirement is necessary for improving the estimate of surface aerosol mass concentration from the satellite-measured radiances or retrieved AODs. Although the UV radiance at the top-of-atmosphere (TOA) is known to be sensitive to centroid height of absorbing aerosols [7], several methods were proposed recently to retrieve centroid height of aerosols, in particular, the scattering aerosols, from O_2 *A* band measurements [25,52]. The physical principle underlying UV aerosol retrieval uses the known profile of Rayleigh scattering to calibrate the profile of aerosol absorption. In contrast, the reasoning behind the O_2 *A* method is to use the profile of O_2 absorption to calibrate the profile of aerosol scattering. However, land surface reflectance is often much higher in the O_2 *A* band than in the UV, and this can weaken the signal of aerosol scattering in upwelling radiance at TOA (see discussion of Fig. 7 below). Consequently, while Butz et al. [53] described the exploratory use of measurements in the O_2 *A* band from Greenhouse gases Observing SATellite (GOSAT [54,55]) to retrieve aerosol plume height globally, promising results (with independent validation) of aerosol centroid height retrieval from O_2 *A* band so far are found for ocean scenarios [9]. To overcome this limitation, Zeng et al. [25] suggested the use of polarization measurements at TOA, since polarized reflectance at the land surface is often low, and this effect would favor the use of aerosol single scattering to derive aerosol properties.

While the physical principles can be readily understood conceptually, several outstanding questions remain for this use of O_2 *A* band reflectances and DOLP. In this section, we will use UNL-VRTM to conduct some exploratory work related to two issues: (a) the optimal choice of wavelengths in the O_2 *A* band, and (b) the sensitivity of the retrieval as a function of viewing geometries for spherical and non-spherical particles. Both questions are related to sensor design: what are the optimal spectral resolution and wavelength choices, and for which viewing scenarios will the polarization in O_2 *A* band have maximum sensitivity to aerosol height? In this regard, the particle shape needs to be considered, as this can affect the scattering phase matrix and polarization as functions of the scattering angle.

Figs. 7a and b show that as the surface reflectance increases, the DOLP at TOA decreases, while the TOA reflectance increases, both within and outside the O_2 *A* band. This is a consequence of the effect of surface depolarization and increased multiple scattering in the atmosphere due to stronger surface reflectance. Since Rayleigh scattering often induces positive and strong DOLP while spherical aerosols generate negative DOLP (see Fig. 8a), increased scattering by aerosols generally results in less positive DOLP. However, O_2 absorption in the O_2 *A* band suppresses aerosol scattering. Hence, the lower the aerosol peak height, the more aerosol scattering is suppressed, and Rayleigh scattering above the aerosol layer contributes more to the DOLP. This effect explains the drop in DOLP inside the O_2 *A* band as the aerosol peak height increases (Fig. 7b). More interestingly, the rate of this decrease with respect to the increase of aerosol peak height appears insensitive to the surface reflectance, although the absolute value of this decrease appears to be larger as surface reflectance increases. The latter effect can be understood as follows: multiple scattering between the surface and atmosphere is always suppressed by the O_2 absorption, and hence, the larger the surface reflectance, the greater are the differences or the changes of DOLP from within the O_2 *A* band to the continuum outside the band. Furthermore, the contrast between Fig. 7b (for O_2 absorption depth of 70) and 7c (for O_2 absorption depth of 133) shows that DOLP at different O_2 *A* absorptions has different sensitivity to aerosol peak height. The larger (smaller) the O_2 absorption optical depth, the greater (lower) the sensitivity of the DOLP to high-elevation aerosols, and the lower (greater) the sensitivity to low-altitude aerosols. At large O_2 absorption optical depth, radiation is prevented from reaching the surface and interacting with aerosols in the lower troposphere (Figs. 7d and 2a). Therefore, two or more measurements of DOLP in the O_2 *A* band that encompass a range of O_2 absorption depth are recommended for retrieval of aerosol peak heights at various altitudes.

Sensitivity patterns of DOLP for the O_2 *A* band with respect to the aerosol peak height (as shown in Figs. 7b and c) are in contrast with reflectance sensitivity patterns (Figs. 7e and f). In the latter, the ratios of O_2 *A* band reflectances to those in the continuum outside the band in general increase as the aerosol peak height rises, reflecting lower O_2 absorption and more aerosol scattering. However, this sensitivity drops off as the surface reflectance increases, because larger surface reflectance often smears the aerosol contribution to the reflectance at the TOA. However, this does show that differences between reflectivity inside the O_2 *A* band and outside the band have some sensitivity to *high-elevation* aerosols, even when surface reflectance is high.

To further evaluate the sensitivity of DOLP and intensity to the aerosol plume height as a function of wavelength, we present in Fig. 7g and h respectively the quantities $\partial \mathrm{DOLP}/\partial \ln H$ and $|\partial \ln DOLP/\partial \ln H| - |\partial \ln I/\partial \ln H|$. Here, calculation of $\partial \mathrm{DOLP}/\partial \ln H$ is done through

$$\frac{\partial \mathrm{DOLP}}{\partial \ln H} = \frac{Q}{I^2}\frac{\partial I}{\partial \ln H} - \frac{1}{I}\frac{\partial Q}{\partial \ln H} \tag{15}$$

Contributions on the right side of Eq. (15) are all readily available after running UNL-VRMT once. Fig. 7g indicates that the DOLP alone has larger sensitivity for relative change of aerosol plume height at higher altitude in the O_2 *A* spectrum, and for the aerosols layers at the same altitude, the DOLP at the edge of O_2 *A* band appears to have larger sensitivity to the change of height than DOLP in the center of the band. However, regardless of the altitude of the aerosol layer, the DOLP at a particular wavelength in the O_2 *A* band overall has *relatively* larger sensitivity to the relative change of plume height than that of intensity (Fig. 7h). This clearly indicates that the measurement of polarization in O_2 *A* band has much more information content for aerosol plume height than does the intensity measurement alone, especially when considering that the accuracy of polarization measurements is also higher [10].

In Fig. 8, we consider the effect of scattering angle and aerosol shape on the sensitivity of DOLP to aerosol peak height. In general for the aerosol properties studied here,

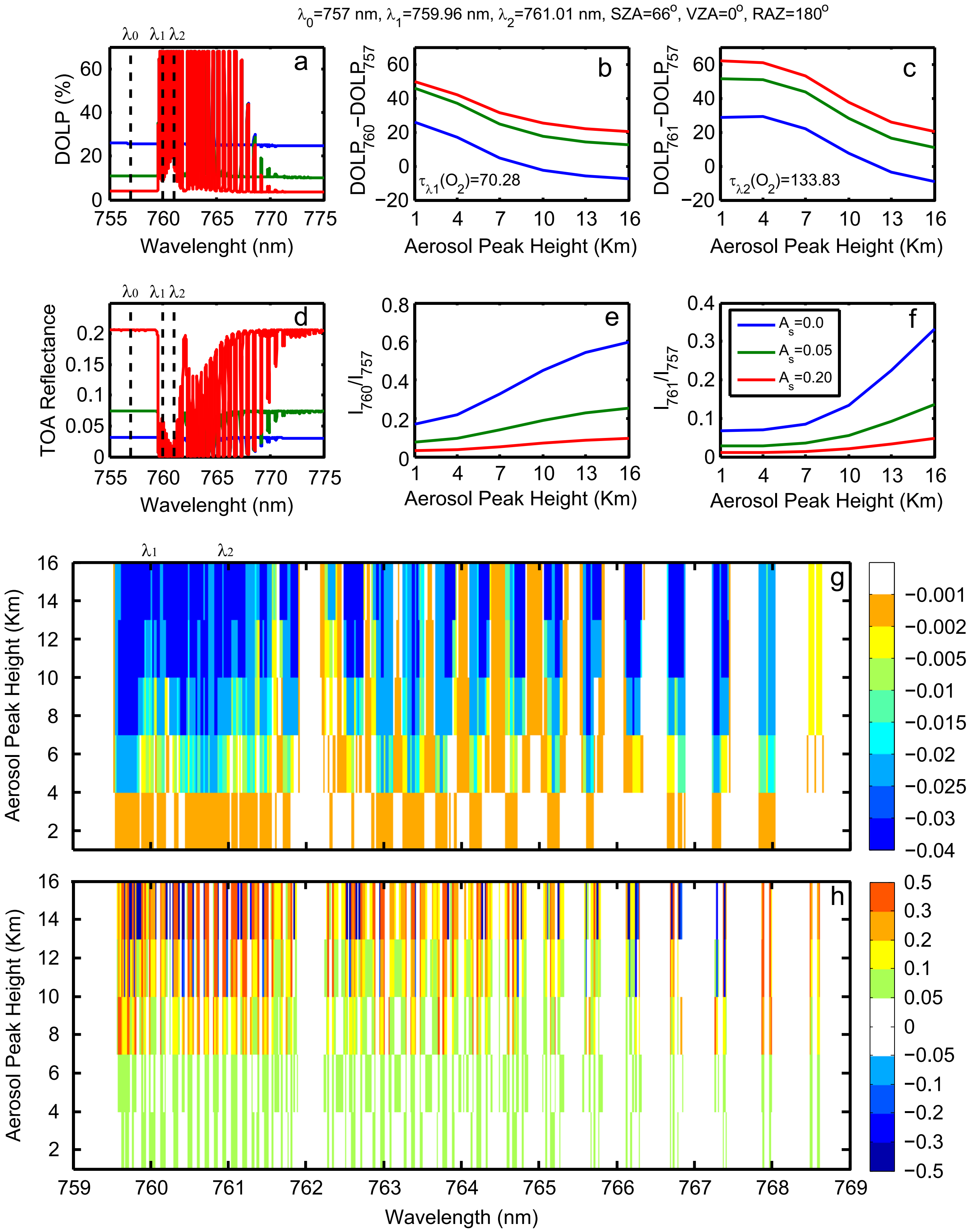

Fig. 7. (a) Simulated DOLP, and (d) normalized radiances (i.e, assuming incoming solar irradiance of unity, bottom row) in the spectral range of 755–775 nm at the top-of-atmosphere for 3 surface reflectances (A_s) respectively of 0 (blue line), 0.05 (green line), and 0.2 (red line). The aerosol altitude is set at 7 km, and aerosols are assumed spherical with lognormal size distribution having $r_g = 0.5$ μm and $\sigma_g = 0.2$ μm, and with refractive index 1.53–0.008*i*. Plots (b) and (c) respectively show the changes of DOLP at two O_2 *A* band wavelengths (λ_1 and λ_2) with respect to the DOLP value in the continuum (λ_0). Plots (e) and (f) are respectively the same as (b) and (c), but for the change of reflectance. Plot (g) shows the moving averages of Jacobians of DOLP with respect to relative change of aerosol height ($\partial DOLP/\partial lnH$), while plot (h) shows the moving averages of the differences of absolute values of normalized Jacobians between DOLP and I with respect to the relative change of height ($|\partial \ln DOLP/\partial \ln H| - |\partial \ln I/\partial \ln H|$). See text for details.

we find that outside of the O_2 *A* band, the DOLP shows nearly zero sensitivity to the aerosol peak height, and the variation of DOLP with scattering angle can be explained by the composite effect of Rayleigh and aerosol single scattering properties. For scattering angles in the range 140–170°, DOLP is negative, since the effect of aerosol multiple scattering (negative DOLP, Fig. 8b) outweighs that for Rayleigh scattering (optical depth = 0.025). However, as the scattering angle moves to lower values (and also toward the backscatter region), the DOLP for spherical particles decreases to near zero, while DOLP for Rayleigh scattering becomes larger toward the scattering angle of 120°, and closer to zero as the scattering angle approaches 180°. Thus the DOLP overall becomes larger and more positive as the scattering angle moves from 140° to 120°, and approaches zero as the scattering angle increases

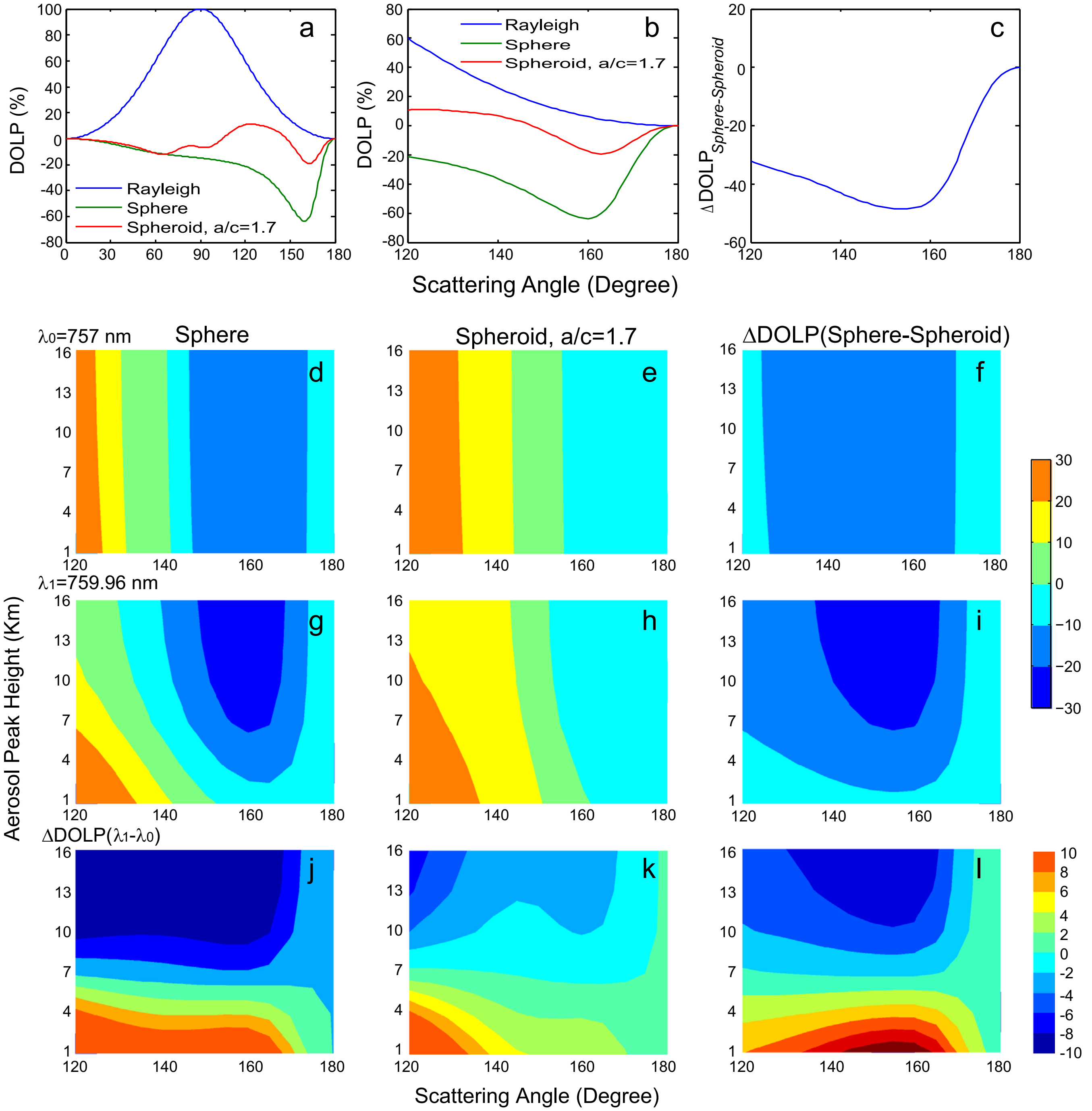

Fig. 8. Analysis of DOLP at the TOA for spherical and non-spherical particles, as well as their differences as a function of scattering angle and aerosol peak height. Plot (a) shows DOLP ($-P_{12}/P_{11}$) for Rayleigh scattering, spherical aerosols, and non-spherical aerosols. The aerosol properties for both spherical and non-spherical particles have the same size distribution and refractive index as those used in Fig. 7. Spheroidal particles are assumed to have an aspect ratio of 1.7. (b) is the same as (a), but for scattering angles 120–180°. Plot (c) is similar to (b) but showing the difference of DOLP between spherical and spheriod particles. Plot (d) is simulated DOLP at the TOA for spherical particles as a function of scattering angle and aerosol peak height, wavelengths outside the *A* band. Plot (g) is similar to (d) but inside the O_2 *A* band. Plot (j) shows the difference between (g) and (d). Plots (e), (h), and (k) are respectively similar to (d), (g), and (j), but for spheroidal particles. Plots (f), (i), and (l) show the differences between (d) and (e), (g) and (h), and (j) and (k) respectively.

above 170° to 180°. In general, patterns of DOLP within the O_2 *A* band (Fig. 8g) follow those observed outside the band (in terms of positive and negative DOLP), except for scattering directions where Rayleigh scattering is important for DOLP (e.g., 120–140°). In this range, DOLP shows high sensitivity to the aerosol peak height. When the aerosols reside at high altitude, O_2 absorption suppresses both Rayleigh and aerosol scattering, and so the positive DOLP found outside the band is diminished (Fig. 8j). As the aerosol layer moves to a lower altitude, DOLP at TOA depends more on Rayleigh scattering above the aerosol layer (and less on aerosol scattering), and therefore, more positive DOLP values become apparent (Fig. 8j). Hence, except for the scattering angle range of 170–180°, DOLPs at other scattering angles are sensitive to aerosol peak height, especially below 10 km. As noted above, higher sensitivity will be apparent for high-altitude aerosols at wavelengths where O_2 absorption is large.

The DOLP patterns with respect to scattering angle for spheroidal particles are in general similar to those for spherical particles, except that the positive DOLP contribution from Rayleigh scattering has a relatively larger contribution, since DOLP for spheroids is small (either positively or negatively). Because the DOLP for scattering by spheroids is typically closer to that for the Rayleigh DOLP as compared to the case for spherical particles [56], the DOLP is only sensitive to high-elevation aerosols at angles where DOLP differences are relatively larger.

Finally, aerosol shape has some impact on the DOLP, especially at 120–170°, both within and outside the O_2 *A* band (Figs. 7f and i). In general, because spheroidal scatter generates small negative and sometimes positive DOLP compared with large negative DOLP values for spherical particle scattering, there is less decrease of DOLP as compared to the case for spheres (Figs. 7f and i). Hence, it is important to account for aerosol non-sphericity when using DOLP to retrieval aerosol peak height.

4.2. Information content analysis for GEO constellation for aerosol retrievals

Although it has not been decided whether GEO-CAPE will have the capability to measure the DOLP in and around the O_2 *A* band, Geostationary satellite (GEO) constellations for remote sensing of aerosols have been proposed and supported by various studies [51]. The GEO satellites TEMPO [64] and GOES-R [57] are expected to be launched in 5 years. Here, we will use our testbed to study the potential of combining measurements from two viewing angles, one from TEMPO and one from GOES-R, with an objective of improving retrieval of aerosol properties (Fig. 9). It has been shown that the combination of measurements from two or more viewing angles from the same sensor aboard a polar-orbiting satellite (such as MISR or ATSR) can generate additional information for characterizing the aerosol properties [4,58]. From geostationary orbit, TEMPO and GOES-R can view the same scene from two different but constant viewing angles (Fig. 9). To explore this synergy, we select 3 visible wavelengths from GOES-R (470, 640, and 860 nm) and 4 wavelengths from TEMPO (340, 380, 470, and 640 nm). Note that although TEMPO is a spectrometer, the 4 wavelengths selected here are atmospheric window channels that either overlap with GOES-R or were used in the past for aerosol retrievals (by OMI). In the information content and error analysis, we assume 100% a priori uncertainty in the column AOD and fine-modal fraction (FMF of AOD, or f_τ). Observation error is defined to include instrument error and forward modeling error. We specify 3% uncertainty for instrumental error. For forward modeling error, we account for errors in the TOA radiances simulation propagated from the errors in the surface BRDF parameters (20% uncertainty) and aerosol single scattering albedos (uncertainty of 0.03 for both size modes).

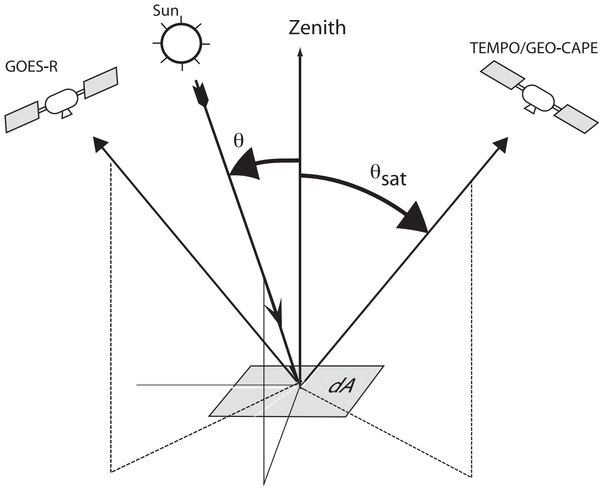

Fig. 9. GEO constellation concept for aerosol retrievals. GOES-R is planned to be located at 135° W over the equator, while TEMPO is planned to be at 100° W above the equator. For the same surface location in the western continental U.S., the viewing angles (θ_{sat}) for both GOES-R and TEMPO will be constant, regardless of the solar zenith angle (θ).

Overall, the DFS values for the retrieval of AOD from GOES-R (Fig. 10a) and TEMPO (Fig. 10b) are found to be higher than 0.9, thus suggesting that both sensors can be used to retrieve AOD, provided that aerosol single scattering properties for both fine and coarse-mode aerosols are defined. However, at viewing directions close to the solar beam (e.g., viewing zenith angle or VZA closer to 40° and relative azimuth angle (RAZ) at 180°), the DFS is reduced for both sensors, especially for GOES-R with DFS values are less than 0.8 and a posterior uncertainty reach as larger as 30% (Fig. 10d). This decrease is due in part to the effect of surface BRDF on retrieval; the surface reflectance is generally larger at directions close to that of the incoming solar beam, and this smears the aerosol scattering signal at TOA and results in the larger uncertainty (lower DFS) in the retrieval. However, because surface reflectance in the UV is generally much lower than that in the visible, the BRDF effect on aerosol retrieval in the UV is smaller than that in the visible. Consequently, for GOES-R that has the shortest wavelength at 470 nm in the visible, the decrease of DFS is large and distinct (Fig. 10a). In contrast, for TEMPO with its UV channels, the decrease of DFS is less significant although still discernable (Fig. 10b). Combining TEMPO and GOES-R thus increases DFS for all geometries and minimizes the effect of BRDF on the aerosol retrievals (Fig. 10c), and a posterior uncertainty are reduced to be less than 10% for any geometry (Fig. 10f).

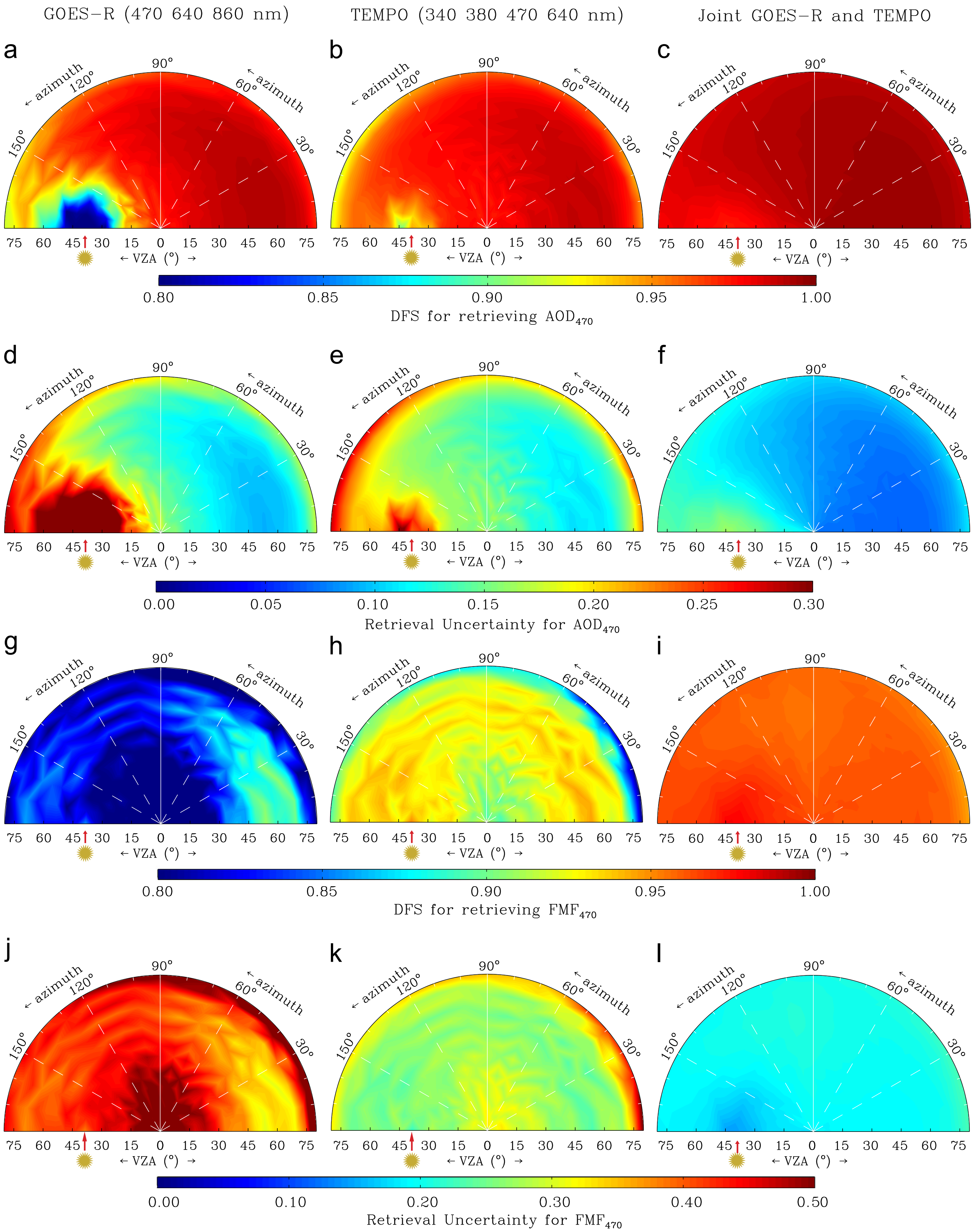

Fig. 10. Polar plots of Degree of Freedom for Signal (DFS) for the retrieval of the total aerosol optical depth at 470 nm (AOD_{470}) from: (a) GOES-R, (b) TEMPO, and (c) joint measurements of GOES-R and TEMPO. Plots (d)–(f) are retrieval uncertainties for AOD_{470} from these three sets of measurements, respectively. Plots (g)–(l) are similar to (a)–(f) but apply to the retrieval of 470 nm AOD fine-modal fraction (FMF_{470}). Note that the three atmospheric window channels from TEMPO are the ones used by AERONET to measure AOD. In each polar plot, the VZA is shown as the radius, while the polar angle represents the relative azimuth. The solar zenith angle is fixed at 40°. Values for joint retrieval correspond to the VZA for GOES-R and averages for different sets of VZA for TEMPO. The two modes are for sulfate- and dust-like aerosols with optical depths of 0.78 and 0.28 respectively at 470 nm. An underlying grass surface is assumed, with MODIS-retrieved BRDF parameters.

Although the retrieval of AOD is now the mainstay for nearly all sensors that measure radiances in the UV and visible, challenges still remain for retrieval of fine-mode AOD. Both multispectral (such as MODIS) and multi-angle (e.g., MISR) measurements can be used to retrieve fine-mode AOD. However each has its limitation – MODIS lacks multi-angle and UV capabilities, while MSIR lacks the wide spectral coverage. From this perspective, TEMPO and GOES-R are complementary in terms of spectral coverage, and their combination can offer the two-angle observation capability. Fig. 10g shows that for most of the expected geometrical configurations, the DFS for GOES-R to retrieve fine-modal fraction (FMF) of AOD is in the range 0.8–0.9. In contrast, for TEMPO (Fig. 10h), the DFS for retrieving fine-mode AOD is mostly larger than 0.9. This contrast is in part due to low surface reflectance at the UV as well as use of 4 channels for TEMPO (as opposed to 3 channels with GOES-R). However, DFS at the nadir appears to be lower for both sensors, as the path length is small at nadir. Interestingly, it appears that BRDF has no distinct effect on the retrieval FMF, at least for the cases analyzed here; this can be understood that the retrieval sensitivity for separating fine- and coarse-mode aerosols depends strongly on the range of the wavelengths selected for the retrieval as well as the composition of their phase functions. Hence, combining TEMPO and GOES-R increases DFS at all geometries (Fig. 10i), reducing uncertainty for FMF from 40% for GOES-R (Fig. 10j) and 30% for TEMPO (Fig. 10k) to 20% (Fig. 10l). It is thus clear that the synergy between TEMPO and GOES-R can minimize the surface BRDF effect on AOD retrieval and improve the fine-mode AOD retrieval overall, especially for GOES-R.

5. Summary and discussions

The past few decades have seen rapid and advanced developments in the linearized computer codes for radiative transfer and particle scattering, hyperspectral databases for molecular spectroscopy, and optimization theory for inversion of geophysical parameters from remote sensing measurements. Following and integrating these developments, we have presented in this paper a numerical testbed for remote sensing of aerosols. The testbed consists of two parts. The first part is the UNL-VRTM model that integrates the linearized codes for computing vector radiative transfer (VLIDORT), and scattering of spherical (LMIE) and non-spherical particles (LTMATRIX); the second part is inverse-model codes that analyze the information content for the retrieval parameters for any given set of synthetic data generated from UNL-VRTM. Benchmark calculations with UNL-VRTM were conducted from the UV to the shortwave infrared (4000 nm). It was shown that the UNL-VRTM is not only able to compute the four Stokes parameters and degree of linear polarization with high accuracy and at high spectral resolution, but also to simultaneously and analytically generate sensitivities of these four Stokes parameters with respect to aerosol parameters of both the fine and coarse modes. The latter capability, when combined with the inverse codes (second part of the testbed), allows us to make an objective analysis of the information content (retrieval uncertainty and DFS) of different aerosol parameters in the synthetic data computed from the forward model. By inclusion of HITRAN and other molecular spectroscopy data for atmospheric trace gases, the UNL-VRTM is also able to perform line-by-line calculation of gas absorption, thus providing another opportunity for the future study of the effect of absorbing gases (such as SO_2, NO_2 and water vapor) on the aerosol retrieval. For a pollution scenario, we have shown that absorption of SO_2 and NO_2 make an important contribution to the optical depth of the atmospheric column and should be properly accounted for in order to retrieve AOD accurately.

A demonstration of the testbed was presented for the design of algorithms for aerosol retrievals to meet the requirement of the NASA's GEO-CAPE mission. Two cases were studied. The first case analyzed the sensitivity of intensity and polarization in the O_2 *A* band to the vertical profile of aerosols. Although this sensitivity was shown to vary with scattering angle, wavelength, aerosol shape, and surface reflectance, we found that overall, the polarization in the O_2 *A* band has higher sensitivity to the vertical profile of aerosols than that of intensity, especially over the high reflective surface. In the second case, we studied the synergy of TEMPO and GOES-R for a joint retrieval of AOD and fine-mode AOD. It was found that the joint retrieval improves the retrieval of both AOD and fine-mode AOD accuracy; the corresponding AOD and fine-mode AOD uncertainties are reduced respectively from 30% to 10% and from 40% to 20%, thus meeting the requirement of GEO-CAPE for aerosols. The improvement of AOD is especially evident when TEMPO is located in the (reflected) sunlight direct beam, the direction for which the surface bi-directional reflectance (BRDF) is largest.

This study should be viewed as the starting point for the development of a framework for objective assessment of aerosol information content for any real or synthetic measurements (see, e.g., Knobelspiesse et al. [14]). Further development of particle scattering codes for non-spherical particles is essential, especially for large particles that are difficult to handle with current implementations of T-matrix theory. Meanwhile, more evaluations of the testbed (with in situ data) are also needed, including in-depth analyses of the two cases presented here that demonstrated the use of the testbed. Examples include the analysis of the retrieval accuracy due to the uncertainty in the a priori error, and due to the use of different algorithm definition factors (such as a combined use of two consecutive measurements from GEO within 1 hour assuming aerosol single scattering properties remain constant). Finally, the testbed is available upon request.

Appendix A. Derivations of transformation vector for VLIDORT for various aerosol parameters

Let x be an aerosol microphysical parameter. The aerosol extinction and scattering optical thickness (τ_A and δ_A), single scattering albedo (ω_A), and Greek coefficient matrix ($\mathbf{B}_A^j$) are functions of x. However, the gaseous absorption and Rayleigh scattering parameters are independent of x. This appendix outlines the derivations of Eqs. (6) and (7) and the expressions in Tables 2 and 3. First, we transform

Eq. (4) as below.

$$\phi_x = \frac{x}{\tau_L}\frac{\partial \tau_L}{\partial x} = \frac{x}{\tau_L}\frac{\partial(\tau_G+\tau_R+\tau_A)}{\partial x} = \frac{1}{\tau_L}x\frac{\partial \tau_A}{\partial x} \tag{A.1}$$

$$\begin{aligned}\varphi_x &= \frac{x}{\omega_L}\frac{\partial \omega_L}{\partial x} = \frac{x}{\omega_L}\frac{\partial[(\tau_G+\delta_A)/\tau_L]}{\partial x} = \frac{x}{\omega_L}\frac{1}{\tau_L^2}\left[\tau_L\frac{\partial(\tau_G+\delta_A)}{\partial x} - (\tau_G+\delta_A)\frac{\partial \tau_L}{\partial x}\right]\\ &= \frac{x}{\omega_L\tau_L}\frac{\partial \delta_A}{\partial x} - (\tau_G+\delta_A)\frac{x}{\omega_L\tau_L^2}\frac{\partial \tau_A}{\partial x} = \frac{x}{\tau_G+\delta_A}\frac{\partial \delta_A}{\partial x} - \frac{1}{\tau_L}x\frac{\partial \tau_A}{\partial x}\\ &= \frac{1}{\tau_G+\delta_A}x\frac{\partial \delta_A}{\partial x} - \phi_x\end{aligned} \tag{A.2}$$

$$\begin{aligned}\boldsymbol{\Psi}_x^j &= \frac{x}{\mathbf{B}_L^j}\frac{\partial \mathbf{B}_L^j}{\partial x} = \frac{x}{\mathbf{B}_L^j}\frac{\partial[(\tau_G\mathbf{B}_R^j+\delta_A\mathbf{B}_A^j)/(\tau_G+\delta_A)]}{\partial x}\\ &= \frac{x}{\mathbf{B}_L^j}\frac{1}{(\tau_G+\delta_A)^2}\left[(\tau_G+\delta_A)\frac{\partial(\delta_A\mathbf{B}_A^j)}{\partial x} - (\tau_G\mathbf{B}_R^j+\delta_A\mathbf{B}_A^j)\frac{\partial \delta_A}{\partial x}\right]\\ &= \frac{x}{\mathbf{B}_L^j}\frac{1}{\tau_G+\delta_A}\left[\frac{\partial(\delta_A\mathbf{B}_A^j)}{\partial x} - \mathbf{B}_L^j\frac{\partial \delta_A}{\partial x}\right]\\ &= \frac{1}{(\tau_G+\delta_A)\mathbf{B}_L^j}\left[\delta_A\, x\frac{\partial \mathbf{B}_A^j}{\partial x} + (\mathbf{B}_A^j - \mathbf{B}_L^j)\, x\frac{\partial \delta_A}{\partial x}\right]\end{aligned} \tag{A.3}$$

These expressions are linear combinations of $x(\partial\tau_A/\partial x)$, $x(\partial\delta_A/\partial x)$, and $x(\partial\mathbf{B}_A^j/\partial x)$. We can then write them in vector formalism by defining

$$\left[\phi'_x,\ \ \varphi'_x,\ \ \left\langle \boldsymbol{\Psi}'^j_x \right\rangle_{j=0,J}\right]^T = \left[x\frac{\partial \tau_A}{\partial x},\ x\frac{\partial \delta_A}{\partial x},\ \left\langle x\frac{\partial \mathbf{B}_A^j}{\partial x}\right\rangle_{j=0,J}\right]:$$

$$\left[\phi_x,\ \ \varphi_x,\ \ \left\langle \boldsymbol{\Psi}^j_x \right\rangle_{j=0,J}\right]^T = \boldsymbol{\Pi}\left[\phi'_x,\ \ \varphi'_x,\ \ \left\langle \boldsymbol{\Psi}'^j_x \right\rangle_{j=0,J}\right]^T \tag{A.4}$$

where $\boldsymbol{\Pi}$ is a matrix comprising the relevant coefficients, as noted in Eq. (7). Eq. (A.4) or (6) and (7) then acts as a universal formulation for preparing linearized inputs of optical property for VLIDORT. Computation of $[\phi_x,\ \ \varphi_x,\ \left\langle \boldsymbol{\Psi}^j_x \right\rangle_{j=0,J}]$ can then be achieved by the calculation of $[\phi'_x,\ \ \varphi'_x,\ \ \left\langle \boldsymbol{\Psi}'^j_x \right\rangle_{j=0,J}]$ for a given parameter x.

Let us first consider the derivation of $[\phi'_x,\ \ \varphi'_x, \left\langle \boldsymbol{\Psi}'^j_x \right\rangle_{j=0,J}]$ for certain aerosol optical properties in a given atmospheric layer, i.e., τ_A, ω_A, and β_A^k, where β_A^k indicates one of the elements in the kth aerosol scattering Greek matrix $\mathbf{B}_A^k$. For $x=\tau_A$, we have

$$\begin{aligned}\phi'_x &= \tau_A\frac{\partial \tau_A}{\partial \tau_A} = \tau_A\\ \varphi'_x &= \tau_A\frac{\partial \delta_A}{\partial \tau_A} = \tau_A\omega_A\\ \boldsymbol{\Psi}'^j_x &= \tau_A\frac{\partial \mathbf{B}_A^j}{\partial \tau_A} = \mathbf{0}.\end{aligned} \tag{A.5}$$

For $x=\omega_A$, we have

$$\begin{aligned}\phi'_x &= \omega_A\frac{\partial \tau_A}{\partial \omega_A} = 0\\ \varphi'_x &= \omega_A\frac{\partial \delta_A}{\partial \omega_A} = \omega_A\tau_A\\ \boldsymbol{\Psi}'^j_x &= \omega_A\frac{\partial \mathbf{B}_A^j}{\partial \omega_A} = \mathbf{0}.\end{aligned} \tag{A.6}$$

For $x=\beta_A^k$, we have

$$\begin{aligned}\phi'_x &= \beta_A^k\frac{\partial \tau_A}{\partial \beta_A^k} = 0\\ \varphi'_x &= \beta_A^k\frac{\partial \delta_A}{\partial \beta_A^k} = 0\\ \boldsymbol{\Psi}'^j_x &= \beta_A^k\frac{\partial \beta_A^j}{\partial \beta_A^k} = \begin{cases}\frac{\delta_A\beta_A^k}{\beta_L^k} & \text{if } j=k\\ 0 & \text{if } j\neq k\end{cases}\end{aligned} \tag{A.7}$$

Expressions in Table 2 are then derived by substituting Eqs. (A.5)–(A.7) to Eq. (A.4).

Our testbed integrates the VLIDORT with linearized Mie/T-matrix codes, and this combination allows us to generate Stokes vectors and associated analytical Jacobians with respect to aerosol microphysical parameters for two aerosol modes. Thus, we must supply the $[\phi'_x,\ \varphi'_x,\ \left\langle \boldsymbol{\Psi}'^j_x \right\rangle_{j=0,J}]$ quantities for all such parameters. We give an example here, assuming that the aerosols are bimodal, with two lognormal size distributions described by geometric standard deviations (σ_g^s and σ_g^c), geometric median radii (r_g^s and r_g^c), and non-sphericity parameters (ε^s and ε^c) for the fine and coarse modes. We note that ε is available only when non-spherical particles are assumed (T-matrix code is applied). Complex refractive indices are $n_r^s - i\,n_i^s$ and $n_r^c - i\,n_i^c$. Given these microphysical properties, the linearized Mie/T-matrix codes will compute for each mode the scattering and extinction efficiencies (Q_{sca} and Q_{ext}), the set of expansion coefficients ($\mathbf{B}_A^j$) of scattering phase matrix, as well as the derivatives of these quantities with respect to the microphysical properties. For a wide size range of aerosol particles, which enable a ~100% accumulated value for the bi-lognormal probability function, the optical thickness for aerosol extinction and scattering and the associated Greek matrix coefficients within for one atmospheric layer can be calculated through

$$\begin{aligned}\tau_A &= \tau_A^s + \tau_A^c = \frac{3m_A^s Q_{ext}^s}{4\rho_A^s r_{eff}^s} + \frac{3m_A^c Q_{ext}^c}{4\rho_A^c r_{eff}^c}\\ \delta_A &= \delta_A^s + \delta_A^c = \frac{3m_A^s Q_{sca}^s}{4\rho_A^s r_{eff}^s} + \frac{3m_A^c Q_{sca}^c}{4\rho_A^c r_{eff}^c}\\ \mathbf{B}_A^j &= \frac{\delta_A^s\mathbf{B}_A^{s\,j} + \delta_A^c\mathbf{B}_A^{c\,j}}{\delta_A^s + \delta_A^c}\end{aligned} \tag{A.8}$$

We can compute vector $[\phi'_x,\ \ \varphi'_x,\ \ \left\langle \boldsymbol{\Psi}'^j_x \right\rangle_{j=0,J}]$ for a given parameter by differentiating Eq. (A.8). For $x=m_A^s$ as an example

$$\begin{aligned}\phi'_x &= m_A^s\frac{3Q_{ext}^s}{4\rho_A^s r_{eff}^s} = \tau_A^s\\ \varphi'_x &= m_A^s\frac{3Q_{sca}^s}{4\rho_A^s r_{eff}^s} = \delta_A^s\\ \boldsymbol{\Psi}'^j_x &= \frac{\delta_A^s}{\delta_A}(\mathbf{B}_A^{s\,j} - \mathbf{B}_A^j).\end{aligned} \tag{A.9}$$

And similarly, for $x=r_g^s$, we have

$$\phi'_x = \tau_A^s\left(\frac{r_g^s}{Q_{ext}^s}\frac{\partial Q_{ext}^s}{\partial r_g^s} - \frac{r_g^s}{r_{eff}^s}\frac{\partial r_{eff}^s}{\partial r_g^s}\right)$$

$$\varphi'_x = \delta^{\mathrm{s}}_{\mathrm{A}} \left(\frac{r^{\mathrm{s}}_{\mathrm{g}}}{Q^{\mathrm{s}}_{\mathrm{sca}}} \frac{\partial Q^{\mathrm{s}}_{\mathrm{sca}}}{\partial r^{\mathrm{s}}_{\mathrm{g}}} - \frac{r^{\mathrm{s}}_{\mathrm{g}}}{r^{\mathrm{s}}_{\mathrm{eff}}} \frac{\partial r^{\mathrm{s}}_{\mathrm{eff}}}{\partial r^{\mathrm{s}}_{\mathrm{g}}} \right)$$

$$\boldsymbol{\Psi}'^{j}_{x} = \frac{\varphi'_x}{\delta_{\mathrm{A}}} (\mathbf{B}^{\mathrm{s}\,j}_{\mathrm{A}} - \mathbf{B}^{j}_{\mathrm{A}}) + r^{\mathrm{s}}_{\mathrm{g}} \frac{\partial \mathbf{B}^{\mathrm{s}\,j}_{\mathrm{A}}}{\partial r^{\mathrm{s}}_{\mathrm{g}}} \tag{A.10}$$

In a similar fashion, we can obtain the vector $[\phi'_x,\ \varphi'_x,\ \left\langle \boldsymbol{\Psi}'^{j}_{x} \right\rangle_{j=0,J}]$ for other fine-mode aerosol parameters including $\tau^{\mathrm{s}}_{\mathrm{A}}$, $\omega^{\mathrm{s}}_{\mathrm{A}}$, $m^{\mathrm{s}}_{\mathrm{A}}$, $n^{\mathrm{s}}_{\mathrm{i}}$, $n^{\mathrm{s}}_{\mathrm{r}}$, $\sigma^{\mathrm{s}}_{\mathrm{g}}$, $r^{\mathrm{s}}_{\mathrm{g}}$, and ε^{s} (as listed in Table 3). For coarse-mode aerosol parameters, the derivations are the same with superscript ‘s’ replaced by ‘c’.

We have implemented various aerosol-loading vertical profiles into the testbed, including uniform, exponential-decreasing, and quasi-Gaussian profile shapes. For the uniform profile, aerosols are assumed evenly distributed with height. The layer AOD for the exponential-decreasing profile follows form

$$\int_{+\infty}^{z} \tau_{\mathrm{A}}(z)\mathrm{d}z = \tau_{\mathrm{A}0} \exp\left(-\frac{z}{H}\right) \tag{A.11}$$

where $\tau_{\mathrm{A}0}$ is the columnar AOD, and H is a scale height parameter. The quasi-Gaussian profile is derived from a generalized distribution function

$$\tau_{\mathrm{A}}(z) = K \frac{\exp(-\gamma |z - z_{\mathrm{peak}}|)}{[1 + \exp(-\gamma |z - z_{\mathrm{peak}}|)]^2} \tag{A.12}$$

where K is a constant related to $\tau_{\mathrm{A}0}$, γ is a half-width constant, and z_{peak} is the height having peak loading. Derivatives of layer aerosol optical thickness with respect to the 3 profile parameters H, γ, and z_{peak} are also included in order to calculate Jacobians of Stokes vector to these parameters, and the vectors $[\phi'_x,\ \varphi'_x,\ \langle \boldsymbol{\Psi}'^{j}_{x} \rangle_{j=0,J}]$ for these derivatives are also shown in Table 3.

Acknowledgement

Funding for this study was provided by the NASA Earth Science Division as part of GEO-CAPE mission study and Glory mission science activities. J. Wang is grateful to Jassim (Jay) A. Al-Saadi and Hal H. Maring for their support, and thanks the GEO-CAPE aerosol working group and science working group for their constructive suggestions and fruitful discussions. The Holland Computing Center of University of Nebraska – Lincoln and NASA High End Computing program are acknowledged for their help in computing.

References

[1] Kaufman YJ, Tanre D, Boucher O. A satellite view of aerosols in climate systems. Nature 2002;419:215–23.

[2] Remer LA, Kaufman YJ, Tanré D, Mattoo S, Chu DA, Martins JV, et al. The MODIS aerosol algorithm, product, and validation. J Atmos Sci 2005;62:947–73.

[3] Levy RC, Remer LA, Mattoo S, Vermote EF, Kaufman YJ. Second-generation operational algorithm: retrieval of aerosol properties over land from inversion of Moderate Resolution Imaging Spectroradiometer spectral reflectance. J Geophys Res 2007;112: D13211. http://dx.doi.org/10.1029/2006JD007811.

[4] Kahn R, West R, McDonald D, Rheingans B. Sensitivity of multiangle remote sensing observations to aerosol sphericity. J Geophys Res 1997;102:16861–70.

[5] Kalashnikova OV, Kahn R. Ability of multiangle remote sensing observations to identify and distinguish mineral dust types: 2. Sensitivity over dark water. J Geophys Res 2006;111:D11207. http://dx.doi.org/10.1029/2005JD006756.

[6] Martonchik JV, Kahn RA, Diner DJ. Retrieval of Aerosol properties over land using MISR observations. In: Kokhanovsky AA, de Leeuw G, editors. Satellite aerosol remote sensing over land. Berlin: Springer; 2009.

[7] Torres O, Tanskanen A, Veihelmann B, Ahn C, Braak R, Bhartia PK, et al. Aerosols and surface UV products from Ozone Monitoring Instrument observations: an overview. J Geophys Res 2007;112: D24S47. http://dx.doi.org/10.1029/2007JD008809.

[8] Tanré D, Bréon FM, Deuzé JL, Dubovik O, Ducos F, François P, et al. Remote sensing of aerosols by using polarized, directional and spectral measurements within the A-Train: the PARASOL mission. Atmos Meas Tech 2011;4:1383–95.

[9] Dubuisson P, Frouin R, Dessailly D, Duforêt L, Léon JF, Voss K, et al. Estimating the altitude of aerosol plumes over the ocean from reflectance ratio measurements in the O2 A-band. Remote Sens Environ 2009;113:1899–911.

[10] Mishchenko M, Cairns B, Kopp G, Schueler CF, Fafaul BA, Hansen JE, et al. Accurate monitoring of terrestrial aerosols and total solar irradiance: introducing the glory mission. Bull Am Meteotrol Soc 2007;88:677–91.

[11] NRC. National Research Council. Earth science and applications from space: national imperatives for the next decade and beyond. Washington, DC: National Academies Press; 2007 (ISBN-13: 978-0-309-14090-4).

[12] Bak J, Kim JH, Liu X, Chance K, Kim J. Evaluation of ozone profile and tropospheric ozone retrievals from GEMS and OMI spectra. Atmos Meas Tech 2013;6:239–49.

[13] Donlon C, Berruti B, Buongiorno A, Ferreira MH, Féménias P, Frerick J, et al. The Global Monitoring for Environment and Security (GMES) Sentinel-3 mission. Remote Sens Environ 2012;120:37–57.

[14] Knobelspiesse K, Cairns B, Mishchenko M, Chowdhary J, Tsigaridis K, van Diedenhoven B, et al. Analysis of fine-mode aerosol retrieval capabilities by different passive remote sensing instrument designs. Opt Express 2012;20:21457–84.

[15] Mishchenko MI, Cairns B, Hansen JE, Travis LD, Burg R, Kaufman YJ, et al. Monitoring of aerosol forcing of climate from space: analysis of measurement requirements. J Quant Spectrosc Radiat Transf 2004;88:149–61.

[16] Rodgers CD, 1996. Information content and optimization of high-spectral-resolution measurements. Paul B. Hays, Jinxue Wang, editors. Proc. SPIE, Optical Spectroscopic Techniques and Instrumentation for Atmospheric and Space Research II, vol. 2830, pp. 136–147.

[17] Dubovik O, Herman M, Holdak A, Lapyonok T, Tanré D, Deuzé JL, et al. Statistically optimized inversion algorithm for enhanced retrieval of aerosol properties from spectral multi-angle polarimetric satellite observations. Atmos Meas Tech 2011;4:975–1018.

[18] Waquet F, Cairns B, Knobelspiesse K, Chowdhary J, Travis LD, Schmid B, et al. Polarimetric remote sensing of aerosols over land. J Geophys Res 2009;114:D01206. http://dx.doi.org/10.1029/2008JD010619.

[19] van Donkelaar A, Martin RV, Spurr RJD, Drury E, Remer LA, Levy RC, et al. Optimal estimation for global ground-level fine particulate matter concentrations. J Geophys Res: Atmos 2013;118:5621–36.

[20] Lenoble J, Remer L, Tanre D. Aerosol Remote Sensing, New York: Springer; 2013.

[21] Kahn RA, Nelson DL, Garay M, Levy RC, Bull MA, Martonchik JV, et al. MISR Aerosol product attributes, and statistical comparisons with MODIS. IEEE Trans Geosci Remote Sens 2009;47:4095–114.

[22] Wang J, Nair US, Christopher SA. Assimilation of satellite-derived aerosol optical thickness and online integration of aerosol radiative effects in a mesoscale model. In: Proceedings of the 13th conference on satellite meteorology and oceanography, 20–24 September 2004. Norfolk, Virginia; 2004.

[23] Xu X, Wang J, Henze DK, Qu W, Kopacz M. Constraints on aerosol sources using GEOS-Chem adjoint and MODIS radiances, and evaluation with multisensor (OMI, MISR) data. J Geophys Res: Atmos 2013;118:6396–413.

[24] Wang J, Xu X, Henze DK, Zeng J, Ji Q, Tsay S-C, et al. Top-down estimate of dust emissions through integration of MODIS and MISR aerosol retrievals with the GEOS-Chem adjoint model. Geophys Res Lett 2012;39:L08802.

[25] Zeng J, Han Q, Wang J. High-spectral resolution simulation of polarization of skylight: sensitivity to aerosol vertical profile. Geophys Res Lett 2008;35:L20801. http://dx.doi.org/10.1029/2008GL035645.

[26] Clarisse L, Coheur PF, Prata F, Hadji-Lazaro J, Hurtmans D, Clerbaux C. A unified approach to infrared aerosol remote sensing and type specification. Atmos Chem Phys 2013;13:2195–221.

[27] Martin RV, Chance K, Jacob DJ, Kurosu TP, Spurr RJD, Bucsela E, et al. An improved retrieval of tropospheric nitrogen dioxide from GOME. J Geophys Res: Atmos 2002;107:4437.

[28] Bodhaine B, Wood NB, Dutton EG, Slusser JS. On Rayleigh optical depth calculations. J Atmos Oceanic Technol 1999;16:1854–61.

[29] Hansen JE, Travis LD. Light scattering in planetary atmospheres. Space Sci Rev 1974;16:527–610.

[30] Spurr R. LIDORT and VLIDORT: linearized pseudo-spherical scalar and vector discrete ordinate radiative transfer models for use in remote sensing retrieval problems. In: Kokhanovsky A, editor. Light scattering review, 3. New York: Springer; 2008.

[31] Rothman LS, Gordon IE, Babikov Y, Barbe A, Chris Benner D, Bernath PF, et al. The HITRAN2012 molecular spectroscopic database. J. Quant. Spectrosc. Radiat. Transf. 2013;130:4–50.

[32] Orphal J, Chance K. Ultraviolet and visible absorption cross-sections for HITRAN. J. Quant. Spectrosc. Radiat. Transf. 2003;82:491–504.

[33] Brion J, Chakir A, Daumont D, Malicet J, Parisse C. High-resolution laboratory absorption cross section of O_3. temperature effect. Chem Phys Lett 1993;213:610–2.

[34] Daumont D, Brion J, Charbonnier J, Malicet J. Ozone UV spectroscopy I: absorption cross-sections at room temperature. J Atmos Chem 1992;15:145–55.

[35] Malicet J, Daumont D, Charbonnier J, Parisse C, Chakir A, Brion J, et al. spectroscopy. II. Absorption cross-sections and temperature dependence. J Atmos Chem 1995;21:263–73.

[36] Spurr R, Wang J, Zeng J, Mishchenko M. Linearized T-matrix and Mie scattering computations. J Quant Spectrosc Radiat Transf 2012;113:425–39.

[37] Mishchenko M, Travis LD. Capabilities and limitations of a current fortran implementation of the T-matrix method for randomly oriented, rotationally symmetric scatters. J Quant Spectrosc Radiat Transf 1998;60:309–24.

[38] Wanner W, Li X, Strahler AH. On the derivation of kernels for kernel-driven models of bidirectional reflectance. J. Geophys. Res.: Atmos. 1995;100:21077–89.

[39] Lucht W, Schaaf CB, Strah.ler AH. An algorithm for the retrieval of albedo from space using semiempirical BRDF models. IEEE Trans Geosci Remote Sens 2000;38:977–98.

[40] Maignan F, Bréon F-M, Fédèle E, Bouvier M. Polarized reflectances of natural surfaces: spaceborne measurements and analytical modeling. Remote Sens Environ 2009;113:2642–50.

[41] Rodgers CD. Inverse methods for atmospheric sounding: theory and practice. N J: World Sci, Hackensack; 2000.

[42] Hasekamp OP, Landgraf J. Linearization of vector radiative transfer with respect to aerosol properties and its use in satellite remote sensing. J Geophys Res 2005;110:D04203. http://dx.doi.org/10.1029/2004JD005260.

[43] Hasekamp OP, Litvinov P, Butz A. Aerosol properties over the ocean from PARASOL multiangle photopolarimetric measurements. J Geophys Res: Atmos 2011;116:D14204.

[44] Knobelspiesse K, Cairns B, Redemann J, Bergstrom RW, Stohl A. Simultaneous retrieval of aerosol and cloud properties during the MILAGRO field campaign. Atmos Chem Phys 2011;11:6245–63.

[45] Ricchiazzi P, Yang S, Gautier C, Sowle D. SBDART: a research and teaching software tool for plane-parallel radiative transfer in the Earth's atmosphere. Bull Am Meteorol Soc 1998;79:2101–14.

[46] Coulson ADP. Polarization and intensity of light in the atmosphere. Hampton: VA A Deepak Pub; 291–3.

[47] Coulson KL, Dave JV, Sekera Z. Tables related to radiation emerging from a planetary atmosphere With Rayleigh scattering. Berkeley, CA: Univ California Press; 1960.

[48] Evans KF, Stephens GL. A new polarized atmospheric radiative transfer model. J Quant Spectrosc Radiat Transf 1991;46:413–23.

[49] Vijay N, Hovenier JW. Polarized light reflected and transmitted by thick Rayleigh scattering atmospheres. Astrophys J 2012;748:28.

[50] Garcia RDM, Siewert CE. The FN method for radiative transfer models that include polarization effects. J Quant Spectrosc Radiat Transf 1989;41:117–45.

[51] Fishman J, Iraci LT, Al-Saadi J, Chance K, Chavez F, Chin M, et al. The United States' next generation of atmospheric composition and coastal ecosystem measurements: NASA's Geostationary Coastal and Air Pollution Events (GEO-CAPE) mission. Bull Am Meteorol Soc 2012;93:1547–66.

[52] Stam DM, De Haan JF, Hovenier JW, Stammes P. Degree of linear polarization of light emerging from the cloudless atmosphere in the oxygen A band. J Geophys Res 1999;104:16843.

[53] Butz A, Guerlet S, Hasekamp O, Schepers D, Galli A, Aben I, et al. Toward accurate CO_2 and CH_4 observations from GOSAT. Geophys Res Lett 2011;38:L14812.

[54] Crisp D, Fisher BM, O'Dell C, Frankenberg C, Basilio R, Bosch H, et al. The ACOS CO_2 retrieval algorithm – Part II: Global XCO_2 data characterization. Atmos Meas Tech 2012;5:687–707.

[55] Kuze A, Suto H, Nakajima M, Hamazaki T. Thermal and near infrared sensor for carbon observation Fourier-transform spectrometer on the Greenhouse Gases Observing Satellite for greenhouse gases monitoring. Appl Opt 2009;48:6716–33.

[56] Mishchenko MI, Travis LD, Macke A. Scattering of light by polydisperse, randomly oriented, finite circular cylinders. Appl Opt 1996;35:4927–40.

[57] Schmit TJ, Gunshor MM, Menzel WP, Gurka JJ, Li J, Bachmeier AS. Introducing The next-generation advanced baseline imager on GOES-R. Bull Am Meteorol Soc 2005;86:1079–96.

[58] Kalashnikova OV, Garay MJ, Davis AB, Diner DJ, Martonchik JV. Sensitivity of multi-angle photo-polarimetry to vertical layering and mixing of absorbing aerosols: quantifying measurement uncertainties. J Quant Spectrosc Radiat Transf 2011;112:2149–63.

[59] Martonchik JV, Diner DJ, Crean KA, Bull MA. Regional aerosol retrieval results from MISR. IEEE Trans Geosci Remote Sens 2002;40:1520–31.

[60] Lee TF, Miller SD. NASA MODIS previews NPOESS VIIRS capabilities. Weather Forecast 2006;21:649–55.

[61] Winker DM, et al. The CALIPSO mission: a global 3D view of aerosols and clouds. Bull Am Meteorol Soc 2010;91:1211–29. http://dx.doi.org/10.175/2010BAMS30091.

[62] McClatchey RA, Fenn RW, Selby JEA, Volz FE, Garing JS. Optical properties of atmosphere, 3rd ed. AFCRL-72-0497; 1972.

[63] Hess M, Koepke P, Schult I. Optical properties of aerosols and clouds: the software package OPAC. Bull Am Meteorol Soc. 1998;79:831–44.

[64] Chance K, Liu X, Suleiman RM, Flittner DE, Al-Saadi J, Janz SJ. Tropospheric emissions: Monitoring of pollution (TEMPO). Proc. SPIE 2013; 8866, Earth Observing Systems XVIII, 88660D.

[65] Cox C, Munk W. The measurement of the roughness of the sea surface from photographs of the Sun glitter. J Opt Soc Ann 1954;44:838–50.